Received: 5 August 2020 | Revised: 1 April 2021 | Accepted: 23 May 2021

DOI: 10.1002/stc.2803

RESEARCH ARTICLE

WILEY

Robust design of tuned mass damper with hybrid uncertainty

Dawei Li[1] | **Hesheng Tang**[1,2] | **Songtao Xue**[1]

[1]Department of Disaster Mitigation for Structures, College of Civil Engineering, Tongji University, Shanghai, China

[2]State Key Laboratory of Disaster Reduction in Civil Engineering, Tongji University, Shanghai, China

Correspondence
Hesheng Tang, Department of Disaster Mitigation for Structures, College of Civil Engineering, Tongji University, 1239 Siping Rd, Shanghai 200092, China.
Email: thstj@tongji.edu.cn

Funding information
National Natural Science Foundation of China, Grant/Award Number: Grant No. 51178337; Natural Science Foundation of Shanghai, Grant/Award Number: Grant No. 17ZR1431900; National Basic Research Program of China (973 Program), Grant/Award Number: Grant No. 2017YFC0703607; Ministry of Science and Technology of the People's Republic of China, Grant/Award Number: Grant No. SLDRCE19-B-02

Summary

The robust design of a tuned mass damper (TMD) with hybrid aleatory and epistemic uncertainties is proposed in this study. In this method, the aleatory uncertainty involved in the external excitation is represented with the white noise in stochastic theory. The epistemic uncertainties derived from fragmentary statistical data and incomplete preknowledge of structural model and site condition are fully captured with the discrete multi-intervals in evidence theory. In order to overcome the computational bottleneck related to the uncertainty propagation of epistemic uncertainties, a parallel-efficient global optimization (parallel-EGO) method is proposed to approximate the bounds of structural response for joint focal elements. Then, a robustness objective function, with the aim to minimize the worst system response of the primary structure, is presented to search the optimal parameters of TMD. Finally, case studies for a single-degree-of-freedom (SDOF) system and a multi-degree-freedom (MDOF) system validate that the designed TMD not only significantly reduces the worst seismic responses but also improves the robustness of the primary structure.

KEYWORDS

evidence theory, hybrid uncertainty, parallel-EGO, robust design, tuned mass damper

1 | INTRODUCTION

Passive control devices are widely used to eliminate structural system responses and improve structural performances under earthquake and wind excitation. With the simplest format and robust performance, tuned mass dampers (TMDs) have been extensively implemented in real-life applications.[1,2] Significant progress has been made in performance improvement of TMDs.[3,4] On the one hand, advanced elements,[5,6] control strategies,[7–9] and topology configurations[10,11] were developed to enhance the robustness of TMDs. On the other hand, as emphasized in this work, considerable efforts were devoted to develop design methods to improve the performance of TMDs.[12–14]

Since Den Hartog[12] pioneered a closed-form formula of a TMD for an undamped single-degree-of-freedom (SDOF) system, many optimal methods have been proposed to enhance the performance of TMD.[15,16] Later, the inherent damping of primary structure was included by several studies.[17,18] It is worth noting that the closed-form formulas might be not suitable for the heavy mass ratio of a TMD.[19] Alternatively, the optimal design of a TMD for the damped structure has been obtained with numerical optimization methods.[13,20–22] For the methods mentioned above, the optimal results were obtained by assumptions of deterministic structural parameters and external excitations. However, the deterministic assumptions of a structural system and excitation may lead to a considerable reduction of the design

performance.[23,24] Therefore, the so-called robust design of a TMD was highlighted in Zang et al. and Marano et al.[25,26] The probabilistic theory seems a rational way for modeling structural uncertainties[27–32] with sufficient data and perfect priori knowledge. Unfortunately, in the preliminary design stage, the statistical information and prior knowledge may not be sufficient to construct a precise probabilistic distribution. In other words, an excessively optimistic result obtained from probabilistic theory would not afford to extremes or epistemic uncertainties. Alternatively, the non-probability-based robust design of a TMD was developed by the researchers to handle the uncertainty existence with ambiguous, incompleteness, and fuzziness.

In the domain of the non-probability-based robust design of a TMD, endeavors have been conducted, such as by Bhattacharjya and Chakraborty,[33] who developed an interval-based performance indicator to search the optimal parameters of the TMD. Chakraborty and Roy[34] gave an interval-based reliability indicator to optimize the size of a TMD, considering the epistemic uncertainties of a filter model and a structural system. Schmelzer et al. and Adam et al.[35,36] investigated the influences of the interval-based epistemic uncertainties in TMD parameters on the seismic performance primary structure with random set and Tchebycheff's inequality. Marano et al.[37] proposed a fuzzy-based and interval-based optimal framework that modeled the uncertainties of structures and an environment. Mrabet et al.[38,39] presented a performance index and reliability index-based optimal design framework for the uncertainties in a structure system that seemed to have given bounds but not a concrete distribution form. As mentioned above, the fuzzy expression of uncertainty may resort to the precise formulation of the fuzzy numbers of a variable,[40] while the interval model of uncertainties may lead to an overconservative result that loses feasibility for civil engineering.

Apart from two extreme scenarios of uncertainty modeling techniques as mentioned above, other interpretations of epistemic uncertainty were developed that might balance the computational cost and accuracy of uncertainty quantification, such as imprecise probability,[41] probabilistic box,[42] and evidence theory.[43,44] Among these interpretations, evidence theory demonstrates more powerful applicability because its flexible framework depends on a theoretical background. The evidence theory was developed in the recent half century,[43,44] and it could be seen as the transitional state between interval theory and probability theory, as well as the generalized model of possibility theory.[45] With the flexibility of a theoretical body, evidence theory-based uncertainty quantification for dynamic analysis[46] and reliability analysis[47] have been conducted in recent years.

To improve the efficiency of uncertainty propagation in evidence theory framework, the perturbation method,[48] the subinterval Taylor expansion,[35,36] the differential evolution method,[49] and the interval Monte Carlo method[50] have been proposed in recent years. The constraints for these methods are obvious. The perturbation method cannot afford a precise result for the higher level of nonlinear problem, the computational cost of artificial intelligent algorithm increases rapidly with the increase of dimensions, the number of expansion points of Taylor series may trap into an exponential increase for the high-dimensional problems, and the interval Monte Carlo method is constrained by the deficiencies of the interval method and Monte Carlo simulations. Compared with the methods mentioned above, the uncertainty propagation method assisted by the surrogate model can improve the accuracy of computations without the loss of efficacy of the computation effort. Among the developed surrogate models, the kriging model[51,52] is widely used in the uncertainty quantification and optimization domain.[53–55] In this work, active learning function efficient global optimization (EGO) with respect to the kriging model was employed to alleviate the computation burden of epistemic uncertainties with evidence theory. Moreover, we use the parallel computational techniques to enhance the computational performance of the EGO. Then, a parallel-efficient global optimization (parallel-EGO) method has been proposed to overcome the computational cost of the uncertainty quantification of the system response for a structure equipped with a TMD.

This paper aims to develop a robust design method of TMDs that simultaneously accounts for the hybrid aleatory and epistemic uncertainties. Aleatory uncertainty is intrinsically random nature of earthquake occurring, whereas epistemic uncertainty is derived from the incomplete prior knowledge and insufficient statistical information of site condition and structural model. The robust optimization problem is solved by searching the worst performance indicators under the influences of uncertainties. The proposed parallel-EGO is employed to propagate the uncertainties in structural model and external excitation to system response. The remaining parts of this paper are organized as follows: Section 2 gives the basic concepts of equations of motion of a structure equipped with TMD and the evidential representation of the epistemic uncertainties rooted in the structural model and external excitation. The uncertainty quantification with parallel-EGO method is presented in Section 3. The framework of the robust design of the TMD is given in Section 4. Section 5 describes how an SDOF system and a multi-degree-of-freedom (MDOF) system were used to validate the feasibility and efficiency of the proposed method. Conclusions and discussions are listed in Section 6.

2 | HYBRID UNCERTAINTY ANALYSIS OF A TMD SYSTEM

In this section, the stochastic analysis of a structural system equipped with a single TMD is introduced. Then, a brief review of evidence theory and evidential representation of a system response with epistemic uncertainty are given.

2.1 | Governing equations of a structural system equipped with a TMD

In this work, a TMD is installed on the top of structure to mitigate the vibration responses under an earthquake excitation. Without loss of generality,[56] the governing equations of this combined system can be written as follows:

$$\mathbf{M}(\boldsymbol{\alpha})\ddot{\boldsymbol{u}}(\boldsymbol{\alpha},\boldsymbol{\beta},t)+\mathbf{C}(\boldsymbol{\alpha})\dot{\boldsymbol{u}}(\boldsymbol{\alpha},\boldsymbol{\beta},t)+\mathbf{K}(\boldsymbol{\alpha})\boldsymbol{u}(\boldsymbol{\alpha},\boldsymbol{\beta},t)=\boldsymbol{f}(\boldsymbol{\alpha},\boldsymbol{\beta},t), \tag{1}$$

where $\boldsymbol{u}(\boldsymbol{\alpha},\boldsymbol{\beta},t)=[u_{\mathrm{T}}(\boldsymbol{\alpha},\boldsymbol{\beta},t),\boldsymbol{u}_{\mathrm{s}}(\boldsymbol{\alpha},\boldsymbol{\beta},t)]^{\mathrm{T}}$ is the displacement response vector of a structural system equipped with TMD, $u_{\mathrm{T}}(\boldsymbol{\alpha},\boldsymbol{\beta},t)$ and $\boldsymbol{u}_{\mathrm{s}}(\boldsymbol{\alpha},\boldsymbol{\beta},t)$ are respectively the displacement of TMD and structure, and $\ddot{\boldsymbol{u}}(\boldsymbol{\alpha},\boldsymbol{\beta},t)$ and $\dot{\boldsymbol{u}}(\boldsymbol{\alpha},\boldsymbol{\beta},t)$ are the related acceleration and velocity vectors, respectively. The vector $\boldsymbol{f}(\boldsymbol{\alpha},\boldsymbol{\beta},t)$ is the force representation of external excitation, and the time-invariant vectors $\boldsymbol{\alpha}=[\alpha_1,\alpha_2,...,\alpha_N]^{\mathrm{T}}$ and $\boldsymbol{\beta}=[\beta_1,\beta_2,...,\beta_L]^{\mathrm{T}}$ are independent epistemic vectors in structural system and external excitation, respectively. In the expression, N and L denote the dimension of vectors $\boldsymbol{\alpha}$ and $\boldsymbol{\beta}$, respectively. The superscript T denotes the transformation operation. The mass matrix $\mathbf{M}(\boldsymbol{\alpha})$, damping matrix $\mathbf{C}(\boldsymbol{\alpha})$, and stiffness matrix $\mathbf{K}(\boldsymbol{\alpha})$ of a structural system are given as follows[38]:

$$\mathbf{M}(\boldsymbol{\alpha})=\begin{pmatrix}0 & 0\\ 0 & \mathbf{M}_{\mathrm{s}}(\boldsymbol{\alpha})\end{pmatrix}+m_{\mathrm{T}}\boldsymbol{a}\boldsymbol{a}^{\mathrm{T}}\ \mathbf{C}(\boldsymbol{\alpha})=\begin{pmatrix}0 & 0\\ 0 & \mathbf{C}_{\mathrm{s}}(\boldsymbol{\alpha})\end{pmatrix}+c_{\mathrm{T}}\boldsymbol{b}\boldsymbol{b}^{\mathrm{T}}\ \mathbf{K}(\boldsymbol{\alpha})=\begin{pmatrix}0 & 0\\ 0 & \mathbf{K}_{\mathrm{s}}(\boldsymbol{\alpha})\end{pmatrix}+k_{\mathrm{T}}\boldsymbol{b}\boldsymbol{b}^{\mathrm{T}}, \tag{2}$$

where $\mathbf{M}_{\mathrm{s}}(\boldsymbol{\alpha})$, $\mathbf{C}_{\mathrm{s}}(\boldsymbol{\alpha})$, and $\mathbf{K}_{\mathrm{s}}(\boldsymbol{\alpha})$ denote the mass, damping, and stiffness matrixes of primary structure with $n\times n$ elements; m_{T}, c_{T}, and k_{T} denote the mass, damping, and stiffness of the attached TMD; and the vectors $\boldsymbol{a}=[1,0,0,...,0_n]^{\mathrm{T}}$ and $\boldsymbol{b}=[1,-1,0,...,0_{n-1}]^{\mathrm{T}}$ are the location vectors of the mass, damping, and stiffness of the TMD.

2.2 | System response under stochastic excitation with uncertain parameters

In stochastic dynamics,[56] the seismic excitation $\ddot{u}_{\mathrm{g}}(t)$ can be represented by a stationary filtered white noise. Specifically, the Kanai–Tajimi model[57] is used to characterize the properties of site conditions:

$$\begin{aligned}\ddot{u}_{\mathrm{g}}(\boldsymbol{\beta},t)=\ddot{u}_f(\boldsymbol{\beta},t)+\ddot{u}_{\mathrm{w}}(t)=-2\zeta_f(\boldsymbol{\beta})\omega_f(\boldsymbol{\beta})\dot{u}_f(\boldsymbol{\beta},t)-\omega_f^2(\boldsymbol{\beta})u_f(\boldsymbol{\beta},t)\\ \ddot{u}_f(\boldsymbol{\beta},t)+2\zeta_f(\boldsymbol{\beta})\omega_f(\boldsymbol{\beta})\dot{u}_f(\boldsymbol{\beta},t)+\omega_f^2(\boldsymbol{\beta})u_f(\boldsymbol{\beta},t)=-\ddot{u}_{\mathrm{w}}(t)\end{aligned}, \tag{3}$$

where ζ_f and ω_f are the efficient damping ratio and the dominant frequency of the ground, respectively. $\ddot{u}_{\mathrm{w}}(t)$ is stationary Gaussian white noise, and it satisfies the following conditions:

$$\mathrm{Exp}\{\ddot{u}_{\mathrm{w}}(t)\}=0\ \ \mathrm{Exp}\{\ddot{u}_{\mathrm{w}}(t)\ddot{u}_{\mathrm{w}}(t+\tau)\}=S_0\delta(\tau), \tag{4}$$

where $\mathrm{Exp}\{\cdot\}$ is the expectation operator, S_0 is the intensity of a two-sided power spectral density matrix, and $\delta(\tau)$ is the Dirac delta function. Introducing the state vector $\boldsymbol{Y}(\boldsymbol{\alpha},\boldsymbol{\beta},t)=\left[\boldsymbol{u}(\boldsymbol{\alpha},\boldsymbol{\beta},t),u_f(\boldsymbol{\beta},t),\dot{\boldsymbol{u}}(\boldsymbol{\alpha},\boldsymbol{\beta},t),\dot{u}_f(\boldsymbol{\beta},t)\right]^{\mathrm{T}}$, output matrix $\boldsymbol{\Gamma}$, and observation vector $\boldsymbol{Z}(\boldsymbol{\alpha},\boldsymbol{\beta},t)$, the state equation is given in Equation (5):

$$\begin{cases}\dot{\boldsymbol{Y}}(\boldsymbol{\alpha},\boldsymbol{\beta},t)=\mathbf{A}(\boldsymbol{\alpha},\boldsymbol{\beta})\boldsymbol{Y}(\boldsymbol{\alpha},\boldsymbol{\beta},t)+\boldsymbol{B}\ddot{u}_{\mathrm{w}}(t)\\ \boldsymbol{Z}(\boldsymbol{\alpha},\boldsymbol{\beta},t)=\boldsymbol{\Gamma}\boldsymbol{Y}(\boldsymbol{\alpha},\boldsymbol{\beta},t)\end{cases}, \tag{5}$$

where the state system matrix $\mathbf{A}(\boldsymbol{\alpha}, \boldsymbol{\beta})$ and input vector $\boldsymbol{B}$ denote the state system matrix and input vector, respectively. Then, the covariance matrixes $\mathbf{R}_{\boldsymbol{YY}}(\boldsymbol{\alpha}, \boldsymbol{\beta})$ and $\mathbf{R}_{\boldsymbol{ZZ}}(\boldsymbol{\alpha}, \boldsymbol{\beta})$ are computed with the stochastic vibration theory[58]:

$$\begin{aligned}\mathbf{A}(\boldsymbol{\alpha},\boldsymbol{\beta})\mathbf{R}_{\boldsymbol{YY}}(\boldsymbol{\alpha},\boldsymbol{\beta})+\mathbf{R}_{\boldsymbol{YY}}(\boldsymbol{\alpha},\boldsymbol{\beta})\mathbf{A}^{\mathrm{T}}(\boldsymbol{\alpha},\boldsymbol{\beta})+2\pi\boldsymbol{B}S_0\boldsymbol{B}^{\mathrm{T}}=0\\ \mathbf{R}_{\boldsymbol{ZZ}}(\boldsymbol{\alpha},\boldsymbol{\beta})=\boldsymbol{\Gamma}\mathbf{R}_{\boldsymbol{YY}}(\boldsymbol{\alpha},\boldsymbol{\beta})\boldsymbol{\Gamma}^{\mathrm{T}}\end{aligned}. \tag{6}$$

As shown in Equation (6), the covariance matrix $\mathbf{R}_{\boldsymbol{YY}}(\boldsymbol{\alpha}, \boldsymbol{\beta})$ can be estimated by using the numerical solution of the Lyapunov equation.[58] As indicated in Equation (6), the estimation of covariance matrix $\mathbf{R}_{\boldsymbol{ZZ}}(\boldsymbol{\alpha}, \boldsymbol{\beta})$ implies that the parameters related to structural system and filter model are deterministic. To capture the influences of epistemic uncertainties rooted in the structural system and filter model on the seismic performance of the combined structural system, an extension of Equation (6) needs to developed. Herein, the evidence theory is used to represent the sparse uncertain information to capture the worst system responses and avoid excessively conservative quantification results.

2.3 | Evidential representation of the epistemic uncertainty

To formulate the uncertain information with a uniform formula, the uncertain vectors $\boldsymbol{\alpha}$ and $\boldsymbol{\beta}$ are collected as the combined vector $\boldsymbol{\theta} = [\boldsymbol{\alpha}, \boldsymbol{\beta}]^{\mathrm{T}}$. The evidential representation of the uncertain component $\theta_i, i \in \forall [1,N+L]$ consists of the focal element $\theta^{\mathrm{I}}_{i,j_i}$ and the corresponding mass function m_{i,j_i}:

$$\left\{\theta^{\mathrm{I}}_{i,j_i}, m_{i,j_i}\right\} = \left\{\left[\underline{\theta}_{i,j_i}, \bar{\theta}_{i,j_i}\right], m_{i,j_i}\right\},\ \ j_i \in \forall[1,J_i],\ \ i \in [1,N+L], \tag{7}$$

where $\underline{\theta}_{i,j_i}$ and $\bar{\theta}_{i,j_i}$ denote the lower bound (LB) and upper bound (UB) of the focal element $\theta^{\mathrm{I}}_{i,j_i}$ and J_i denotes the number of focal elements of the uncertain component θ_i. According to the evidence theory,[43,44] all of subset $\theta^{\mathrm{I}}_{i,j_i}$ comes from the power set 2^{θ_i} and the related mass function m_{i,j_i} satisfies the following:

$$m(\emptyset) = 0,\ \ m_{i,j_i} \geq 0,\ \ \sum\nolimits_{j_i=1}^{J_i} m_{i,j_i} = 1. \tag{8}$$

The mass function m_{i,j_i} denotes the degree of support of the certain element $\theta_{i,\mathrm{temp}}$ belonging to the subinterval $\theta^{\mathrm{I}}_{i,j_i}$, which can also be called the basic belief assignment (BBA) of $\theta^{\mathrm{I}}_{i,j_i}$. For the construction of the evidential representation of uncertain input, the evidential propagation of uncertainties is conducted. A joint BBA of the uncertain vector is constructed using a Cartesian product:

$$\boldsymbol{\theta}^{\mathrm{I}}_q = \left[\theta^{\mathrm{I}}_{1,j_1}, ..., \theta^{\mathrm{I}}_{i,j_i}, ..., \theta^{\mathrm{I}}_{N+L,j_{N+L}}\right]^{\mathrm{T}},\ \ m_q = \prod\nolimits_{i=1}^{N+L} m_{i,j_i},\ \ q \in \left[1, \prod\nolimits_{i=1}^{N+L} J_i\right], \tag{9}$$

in which $j_i \in \forall [1, J_i]$, $i \in \forall [1,N+L]$, $\boldsymbol{\theta}^{\mathrm{I}}_q$ is the joint focal element of the uncertain input, and m_q is the joint BBA corresponding to $\boldsymbol{\theta}^{\mathrm{I}}_q$. According to the above description, the evidential representation of the covariance for structural response $Z_k(\boldsymbol{\theta}), k \in [1, 2n]$ of interesting can be given by

$$\left\{\left[\underline{R}_{Z_kZ_k}\left(\boldsymbol{\theta}^{\mathrm{I}}_q\right), \bar{R}_{Z_kZ_k}\left(\boldsymbol{\theta}^{\mathrm{I}}_q\right)\right], m_q\right\}, \tag{10}$$

where $\underline{R}_{Z_kZ_k}\left(\boldsymbol{\theta}^{\mathrm{I}}_q\right)$ and $\bar{R}_{Z_kZ_k}\left(\boldsymbol{\theta}^{\mathrm{I}}_q\right)$ denote the LB and UB for focal element $R_{Z_kZ_k}\left(\boldsymbol{\theta}^{\mathrm{I}}_q\right)$. In order to alleviate the computational burden, the parallel-EGO-based uncertainty propagation is implemented. The approximation of the bounds of a system response for each joint focal element was transformed as two optimal problems for searching the minimum and maximum values of the system response.

3 | PARALLEL-EGO-BASED UNCERTAINTY QUANTIFICATION

The kriging model was derived from geological engineering to estimate the distribution of minerals. In combination with the design of experiment (DOE), the kriging model was developed as a surrogate for the complexity and large-scale analysis. A brief summary of the kriging model is introduced in Appendix A, and a more detailed information of kriging is presented in Lophaven et al.[52] The parallel-EGO-based uncertainty propagation and evidential measurement of the system response are given in the following.

3.1 | Evidential uncertainty propagation using parallel-EGO

The EGO algorithm was proposed by Jones et al.[51] to estimate the optimal value of a system response. The EGO provides infill measures for which the observed point is $I(\boldsymbol{x}) = \max\{y_{\min} - \hat{y}(\boldsymbol{x}), 0\}$, where $y_{\min}$ is the minimum value in the current design point set, $\hat{y}(\boldsymbol{x})$ is the estimated value. The expectation improvement (EI) is defined as the maximum value of expectation $\mathrm{Exp}\{I(\boldsymbol{x})\}$. The formulation of EI is expressed as follows:

$$\mathrm{Exp}\{I(\boldsymbol{x})\} = (y_{\min} - \hat{y}(\boldsymbol{x}))\Phi\left(\frac{y_{\min} - \hat{y}(\boldsymbol{x})}{\mathrm{s}(y(\boldsymbol{x}))}\right) + \mathrm{s}(y(\boldsymbol{x}))\phi\left(\frac{y_{\min} - \hat{y}(\boldsymbol{x})}{\mathrm{s}(y(\boldsymbol{x}))}\right), \tag{11}$$

in which $\mathrm{Exp}\{\cdot\}$ denotes the expectation operator, $\Phi(\cdot)$ and $\phi(\cdot)$ denote the cumulative distribution function (CDF) and probability density function (PDF) of the Gaussian distribution, $\mathrm{s}(y(\boldsymbol{x}))$ denotes the square root of $\mathrm{var}(y(\boldsymbol{x}))$. According to the formula as shown in Equation (11), the optimal process using EGO is a sequential DOE of the kriging model. The stop criteria of EGO are set either when the value of $\mathrm{Exp}\{I(\boldsymbol{x})\}$ is less than a threshold value or when a maximum number of steps are reached. The evidential uncertainty propagation is an evaluation processes for searching the maximum and minimum values in each joint focal element $\boldsymbol{\theta}_q^{\mathrm{I}}$. The objective function of the optimization procedure is defined as the system response of interest. Thus, the uncertainty propagation of the system response $\underline{R}_{Z_k Z_k}\left(\boldsymbol{\theta}_q^{\mathrm{I}}\right)$ and $\bar{R}_{Z_k Z_k}\left(\boldsymbol{\theta}_q^{\mathrm{I}}\right)$ can be rewritten in the following:

$$\begin{aligned} \text{find} \quad & \min\left\{R_{Z_k Z_k}\left(\boldsymbol{\theta}_q\right)\right\} \\ \text{s.t.} \quad & \underline{\boldsymbol{\theta}}_q \le \boldsymbol{\theta}_q \le \bar{\boldsymbol{\theta}}_q \end{aligned}, \tag{12}$$

$$\begin{aligned} \text{find} \quad & \max\left\{R_{Z_k Z_k}\left(\boldsymbol{\theta}_q\right)\right\} \\ \text{s.t.} \quad & \underline{\boldsymbol{\theta}}_q \le \boldsymbol{\theta}_q \le \bar{\boldsymbol{\theta}}_q \end{aligned}. \tag{13}$$

With the characters of the evidence theory-based uncertainty propagation, the EGO-based interval optimization can be enhanced using parallel computational works. A detailed procedure of the parallel-EGO-based evidential uncertainty propagation is given in Figure 1.

As shown in Figure 1, the evidence theory-based uncertainty propagation employs a twice parallel-EGO process in each joint focal element to search the LB and UB of system responses. The evaluation process in each joint focal element of the parallel-EGO-based kriging model may use at most hundreds of calls to the performance function. This is meaningful for very high computational demanding simulation models. After the uncertainty propagation, the evidential covariance of a system response is represented as the focal element and mass function, $\left(\left[\underline{R}_{Z_k Z_k}\left(\boldsymbol{\theta}_1^{\mathrm{I}}\right), \bar{R}_{Z_k Z_k}\left(\boldsymbol{\theta}_1^{\mathrm{I}}\right)\right], m_1\right)$, ..., $\left(\left[\underline{R}_{Z_k Z_k}\left(\boldsymbol{\theta}_Q^{\mathrm{I}}\right), \bar{R}_{Z_k Z_k}\left(\boldsymbol{\theta}_Q^{\mathrm{I}}\right)\right], m_Q\right)$.

3.2 | Uncertainty measurement with evidence theory

In evidence theory, the uncertainty measurement of a system response is obtained via two functions, the belief function (*Bel*) and the plausibility function (*Pl*). The *Bel* and *Pl* are respectively used to denote the degree of total belief and degree of partial support for a proposition. The mathematical representation of *Bel* and *Pl* of the system response $R_{Z_k Z_k}(\boldsymbol{\theta})$ for a given threshold value R_{thre} is expressed as follows:

***Step* 1:** Construct joint focal element and corresponding joint BBA using Cartesian product $\left[\boldsymbol{x}_q^{\mathrm{I}}, m_q\right]$
***Step* 2:** Distribute the joint focal element for parallel CPU works
2.1: Initialize the design points set $\mathbf{X}^0 = \left\{\boldsymbol{x}_1^0, \boldsymbol{x}_2^0, \cdots, \boldsymbol{x}_{N_0}^0\right\}$ using Latin hypercube design (LHD).
2.2: Evaluate the each vector $y_i = f\left(\boldsymbol{x}_i^0\right), \boldsymbol{x}_i^0 \in \mathbf{X}^0, y_i \in \mathbf{Y}^0$ and construct the design point set $\{\mathbf{X}^1 = \mathbf{X}^0, \mathbf{Y}^1 = \mathbf{Y}^0\}$ and $\{\mathbf{X}^2 = \mathbf{X}^0, \mathbf{Y}^2 = -\mathbf{Y}^0\}$.
2.3: Find the initial optimal value $y_{\mathrm{best}}^1 = \min(\mathbf{Y}^1)$ and $y_{\mathrm{best}}^2 = \min\left(\mathbf{Y}^2\right)$.
2.4: Determine best observation $\boldsymbol{x}_{\mathrm{best}}^1 \leftarrow \boldsymbol{x} \in \mathbf{X}^1, y(\boldsymbol{x}) = y_{\mathrm{best}}^1$ and $\boldsymbol{x}_{\mathrm{best}}^2 \leftarrow \boldsymbol{x} \in \mathbf{X}^2, y(\boldsymbol{x}) = -y_{\mathrm{best}}^2$
2.5: While the stop criterion is not met.
Construct Kriging model using current design point sets $\{\mathbf{X}^1, \mathbf{Y}^1\}$ and $\{\mathbf{X}^2, \mathbf{Y}^2\}$.
Find $\boldsymbol{x}_{\mathrm{add}}^1 = \mathrm{argmax}\left\{\mathrm{EI}\left(\boldsymbol{x}_{\mathrm{temp}}^1, y_{\mathrm{best}}^1\right)\right\}$ and $\boldsymbol{x}_{\mathrm{add}}^2 = \mathrm{argmax}\left\{\mathrm{EI}\left(\boldsymbol{x}_{\mathrm{temp}}^2, y_{\mathrm{best}}^2\right)\right\}$
Evaluate $y_{\mathrm{add}}^1 = f\left(\boldsymbol{x}_{\mathrm{add}}^1\right)$ and $y_{\mathrm{add}}^2 = -f\left(\boldsymbol{x}_{\mathrm{add}}^2\right)$.
Update $\mathbf{X}^1 = \mathbf{X}^1 \cup \boldsymbol{x}_{\mathrm{add}}^1$ and $\mathbf{X}^2 = \mathbf{X}^2 \cup \boldsymbol{x}_{\mathrm{add}}^2$
Update $\mathbf{Y}^1 = \mathbf{Y}^1 \cup y_{\mathrm{add}}^1$ and $\mathbf{Y}^2 = \mathbf{Y}^2 \cup y_{\mathrm{add}}^2$
Find $y_{\mathrm{best}}^1 = \min(\mathbf{Y}^1)$ and $y_{\mathrm{best}}^2 = \min\left(\mathbf{Y}^2\right)$
Update $\boldsymbol{x}_{\mathrm{best}}^1 \leftarrow \boldsymbol{x} \in \mathbf{X}, y(\boldsymbol{x}) = y_{\mathrm{best}}^1$ and $\boldsymbol{x}_{\mathrm{best}}^2 \leftarrow \boldsymbol{x} \in \mathbf{X}, y(\boldsymbol{x}) = -y_{\mathrm{best}}^2$
End while
***Step* 3:** Build the evidential representation of the system response $\left\{\left[y_{\mathrm{best}}^1, -y_{\mathrm{best}}^2\right], m_q\right\}$.

FIGURE 1 Pseudo-codes of the parallel-EGO-based uncertainty propagation

$$Bel(R_{\mathrm{thre}}) = \sum_{\bar{R}_{Z_kZ_k}\left(\boldsymbol{\theta}_q^{\mathrm{I}}\right) \le R_{\mathrm{thre}}} m_q, \quad Pl(R_{\mathrm{thre}}) = \sum_{\underline{R}_{Z_kZ_k}\left(\boldsymbol{\theta}_q^{\mathrm{I}}\right) \le R_{\mathrm{thre}}} m_q . \tag{14}$$

Then the *Bel* and *Pl* for a series of incremental R_{thre} construct the cumulative belief function (CBF) and cumulative plausibility function (CPF). Therefore, the quantile values of CPF and CBF are transformed to the LB and UB of with quantile probability for a given R_{thre}. Using the statistical moment concept in classical probability theory, the evidential expectation of $R_{Z_kZ_k}$ is formulated as follows:

$$\mathrm{Exp}\{R_{Z_kZ_k}(\boldsymbol{\theta})\} = \left[\sum_{q=1}^{Q} \underline{R}_{Z_kZ_k}\left(\boldsymbol{\theta}_q^{\mathrm{I}}\right) \times m_q, \quad \sum_{q=1}^{Q} \bar{R}_{Z_kZ_k}\left(\boldsymbol{\theta}_q^{\mathrm{I}}\right) \times m_q\right]. \tag{15}$$

As shown in Equation (15), the expectation of performance indicator using the evidential form is obtained, and the corresponding result is represented by the LB and UB.

4 | OPTIMUM TMD PARAMETERS WITH ROBUST DESIGN

In line with above sections, the robust design procedure of a TMD with uncertain parameters is presented in this section. The traditional EGO algorithm was employed to search for the best candidate in design space. In this work, the objective function of the robust design was defined using the first-order statistical moment with evidential representation:

$$\text{object function}: J(\boldsymbol{\eta}, \boldsymbol{\theta}) = \sum_{q=1}^{Q} \bar{R}_{Z_kZ_k}\left(\boldsymbol{\theta}_q^{\mathrm{I}}, \boldsymbol{\eta}\right) \times m_q, \tag{16}$$

where the objective function is the measurement to quantify the worst case of the covariance response under the stochastic excitation. In other words, the optimal result may have captured the extreme scenario of the detuning effect of TMD and the incomplete knowledge of the external excitation. Based on the above considerations, the optimal problem of the TMD parameters is given as follows:

$$\begin{aligned} &\text{find design variable}: && \boldsymbol{\eta} = [\eta_1, \eta_2, ..., \eta_d]^{\mathrm{T}} \\ &\text{minimize}: && J(\boldsymbol{\eta}, \boldsymbol{\theta}) \\ &\text{s.t.} && \underline{\eta}_i \le \eta_i \le \bar{\eta}_i, \quad i \in \forall[1, d] \\ & && m_{\mathrm{T}} = \mu_{\mathrm{T}} m_{\mathrm{s}} \end{aligned} \tag{17}$$

where m_s is the total mass of primary structure, and $\underline{\eta}_i$ and $\bar{\eta}_i$ are the LB and UB with respect to ith design variable η_i. μ_T denotes the mass ratio of the TMD with respect to the total mass of the primary structure. The optimal design process involved two loops of searching for the global optimal value. The inner optimization process, the parallel-EGO method, was used to approximate the UB of the first-order statistical moment as mentioned in Equation (16). In the uncertainty propagation, the Cartesian product was distributed to the parallel-EGO processes, and the results were combined using the uncertainty measurement. Then, the uncertainty quantification result was used to update the training set of the outer loop of the optimal process. In order to illustrate above iterative process, we plotted the complete procedure of the optimal design of the TMD using the evidence theory, as shown in Figure 2.

As indicated in Figure 2, the initial training set of the kriging model was generated using Latin hypercube sampling (LHS)-based DOE. The EGO and parallel-EGO methods started with a small size for the training set, and the train set was enriched step by step. The iterative process illustrated in Figure 2 was dependent on the estimation of the current optimization seed using the parallel-EGO algorithm. It is worth noting that the minimization performance indicator EI could be solved with a differential evolution algorithm for dimensions less than 100. Additionally, Figure 2 shows that

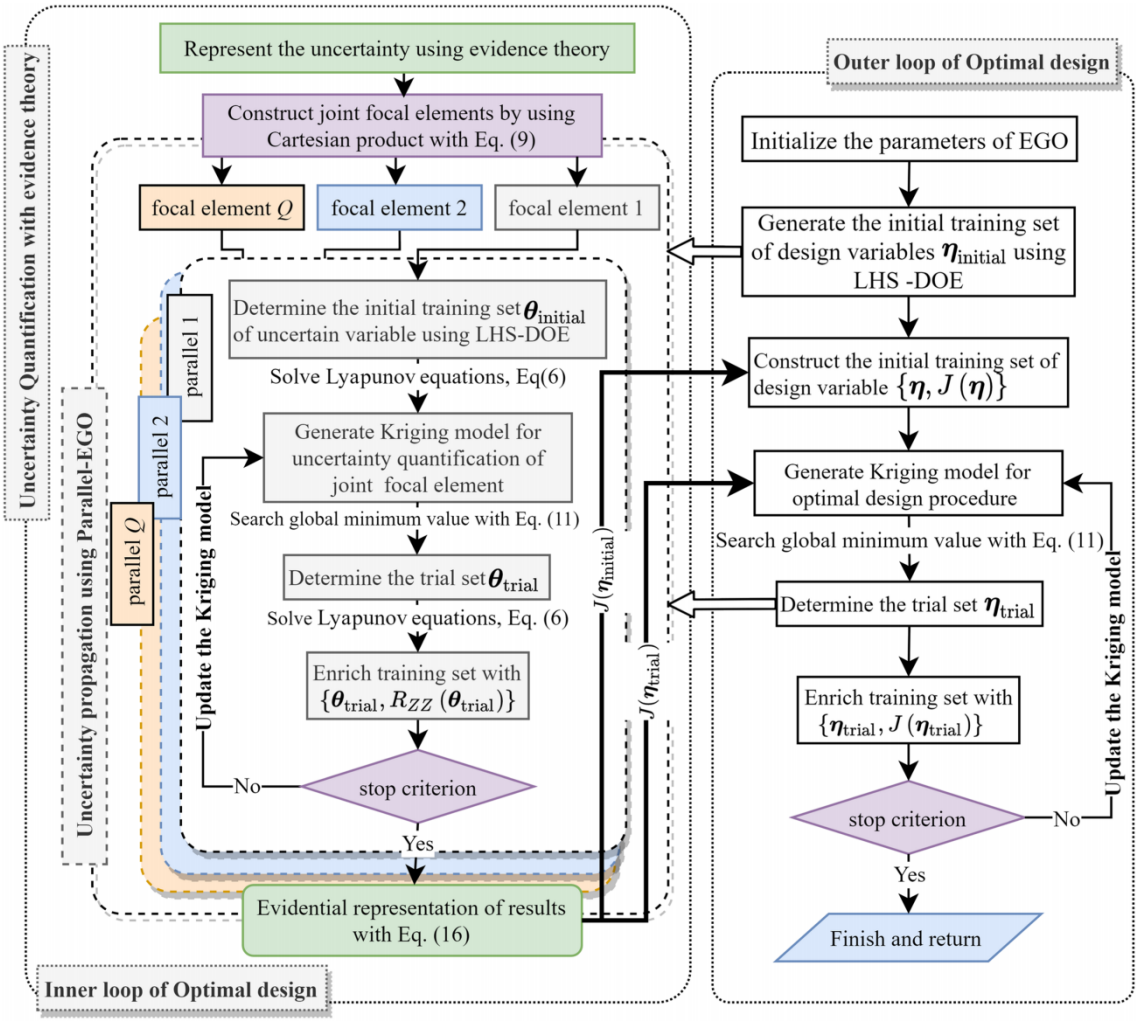

FIGURE 2 Flowchart of the robust design of the TMD with parallel-EGO

the results of the uncertainty quantification were used to enrich the training set of the kriging model for optimal process. The global optimal design result was obtained by judging whether the stop criterion was satisfied. Consider the different degree of uncertain level for each joint focal element, the stop criterion with threshold value of $\mathrm{Exp}\{I(\boldsymbol{x})\}$ may lead to a large divergence of approximation value with respect to the extreme value of system response. Therefore, the stop criterion used in this work was the maximum number iterative generations, namely, $N_{\max} = 100$.

5 | CASE STUDY

As described in this section, an SDOF system and a 10-story benchmark model equipped with a TMD were used to investigate the feasibility and efficiency of the proposed method.

5.1 | Optimal uncertain SDOF system with a TMD

As described in Figure 3, a TMD was installed on the top of an SDOF system to control the displacement response u_s.[34] The seismic input was modeled as the Kanai–Tajimi model,[57] where the dominant frequency ω_f and the damping ratio ζ_f were assumed to be the epistemic uncertainty. The fundamental frequency and the damping ratio of the primary structure were also assumed to be uncertain variables. The detailed information of these variables is listed in Table 1. In the context of the robust design procedure, the mass ratios of the TMD were set as 0.01 and 0.03.

Table 1 shows the uncertain vector of structural system $\boldsymbol{\alpha}^{\mathrm{I}} = [(\omega_s)^{\mathrm{I}}, (\zeta_s)^{\mathrm{I}}]^{\mathrm{T}}$ and the uncertain vector of external excitation $\boldsymbol{\beta}^{\mathrm{I}} = [(\omega_f)^{\mathrm{I}}, (\zeta_f)^{\mathrm{I}}]^{\mathrm{T}}$. The joint focal element of the uncertain system input could be constructed with the Cartesian product, and joint BBA was given as

$$\boldsymbol{\theta}_q^{\mathrm{I}} = \left[(\omega_s)_{j_1}^{\mathrm{I}}, (\zeta_s)_{j_2}^{\mathrm{I}}, (\omega_f)_{j_3}^{\mathrm{I}}, (\zeta_f)_{j_4}^{\mathrm{I}}\right]^{\mathrm{T}}, \quad m_q = m_{j_1} \times m_{j_2} \times m_{j_3} \times m_{j_4}, \quad q \in \forall[1, Q], \tag{18}$$

where $j_i \in \forall\,[1, J_i]$ denotes the number of focal elements of each uncertain variable, $i \in \forall\,[1,4]$ denotes the number of dimensions of the uncertain inputs, and $Q = \prod_{i=1}^{4} J_i = 27$ denotes the number of joint focal elements. Using the above information, the uncertainty propagation process could be conducted using the parallel-EGO algorithm. For the

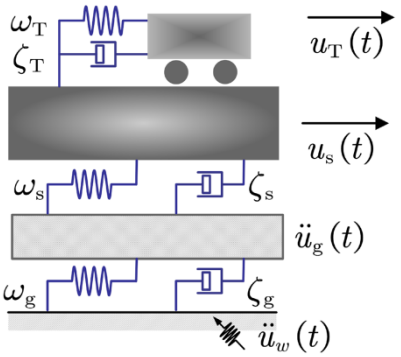

FIGURE 3 SDOF system equipped with TMD

TABLE 1 Evidential representation of the uncertain parameters

ω_s (rad/s)		ζ_s		ω_f (rad/s)		ζ_f	
Focal element	**BBA**	**Focal element**	**BBA**	**Focal element**	**BBA**	**Focal element**	**BBA**
[7.67, 11.86]	0.163	[0.04, 0.06]	1	[10.24, 15.83]	0.156	[0.22, 0.34]	0.176
[11.86, 16.04]	0.680			[15.83, 21.41]	0.687	[0.34, 0.46]	0.678
[16.04, 20.23]	0.157			[21.41, 27.00]	0.157	[0.46, 0.58]	0.146

uncertainty propagation stage, the initial points of the DOE were set as $p = 5 \times 6 = 30$, the iteration stop was set as 70, and the total iterative number was 100. According to the evidential measurements as descripted in Section 3.2, the uncertainty propagation results obtained from the parallel-EGO method are plotted in Figure 4 with $\mathrm{CPF}_{\text{P-EGO}}$ and $\mathrm{CBF}_{\text{P-EGO}}$. To validate the accuracy of the parallel-EGO optimum process, the baseline results were presented with Monte Carlo simulation with 10^5 and 10^6 sampling, respectively. The corresponding uncertainty measure results are plotted in Figure 4, with $\mathrm{CPF}_{\mathrm{MC}_1}$, $\mathrm{CPF}_{\mathrm{MC}_2}$, $\mathrm{CBF}_{\mathrm{MC}_1}$, and $\mathrm{CBF}_{\mathrm{MC}_2}$. Furthermore, Figure 4 shows a probabilistic result with a blank line that is employed to illuminate the relationship between the aleatory uncertainty and epistemic uncertainty. The probabilistic distributions of uncertain parameters ω_s, ω_f, and ζ_f were modeling with norm distribution with coefficients of variation 0.15. The uncertain parameter ζ_s follows uniform distribution ranges from 0.04 to 0.06. Then, the probabilistic result of $R_{u_s u_s,0}(\boldsymbol{\theta})$ was estimated from the Monte Carlo simulation with 10^6 sampling.

Figure 4 shows that the CBF and CPF obtained from the uncertainty propagation with evidence theory envelope the CDF curve obtained from probabilistic model. The gap located between CBF and CPF denotes the incomplete of statistical information of uncertain variables in Table 1. On the other hand, the CDF denotes the uncertainty propagation result obtained from the aleatory uncertainty with perfect knowledge of distribution form and complete statistical information of uncertain variable. It is obviously found that the gap between CBF and CPF reduces to the CDF with the gradual accumulation of uncertain information.

Figure 4 illustrates that the gap between CBF and CPF curves obtained by using Monte Carlo simulations with 10^6 sampling was wider than 10^5 sampling that denotes the accuracy of Monte Carlo simulation is improved with the added the samples. Figure 4 also shows that the parallel-EGO-based propagation result was wider than the Monte Carlo simulation with 10^5 and 10^6 sampling, which means that the parallel-EGO algorithm gave a more accurate uncertainty propagation result than the above Monte Carlo simulations. Additionally, the LB and UB of the expectation of the covariance of the displacement response were given by Equation (15) as $\left[\mathrm{Exp}\{\underline{R}_{u_s u_s,0}(\boldsymbol{\theta})\}, \mathrm{Exp}\{\bar{R}_{u_s u_s,0}(\boldsymbol{\theta})\}\right]$ were $[1.31, 6.83] \times 10^{-3}$, $[1.29, 6.93] \times 10^{-3}$, and $[1.26, 7.11] \times 10^{-3}$ m^2 for Monte Carlo simulations with 10^5 and 10^6 samples and parallel-EGO, respectively.

In addition to investigate the accuracy of the proposed method, the computational efficiency was the other indicator that is considered. The evidence theory-based uncertainty propagation requires 200, 10^5, and 10^6 calls of performance function by employing parallel-EGO and two kinds of Monte Carlo simulations. In this work, a computational server with 18 parallel works, provided by two Intel Xeon CPU E5-4627, was employed to conduct the parallel computation of uncertainty propagations. The Monte Carlo simulation with 10^6 sampling spends 266 s, and the proposed parallel-EGO costs 26 s to finish the uncertainty quantification. With a higher accuracy for approximation of uncertainty influences and smaller numbers of calls to performance function and computational cost, it could be determined that the parallel-EGO-based optimization algorithm was efficient and accurate. Moreover, such a large difference between the LB and

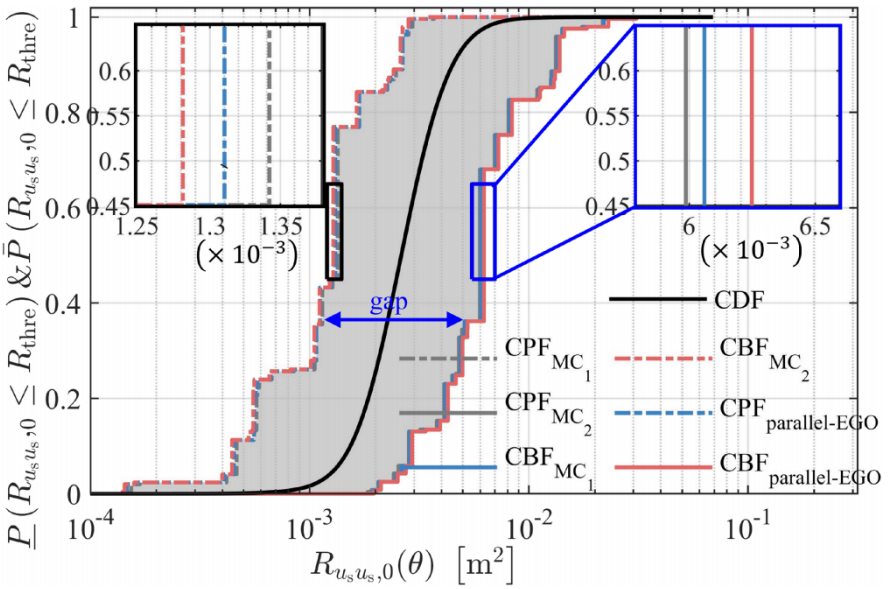

FIGURE 4 Results obtained by parallel-EGO and the Monte Carlo simulations

UB of $\mathrm{Exp}\{R_{u_s u_s,0}(\boldsymbol{\theta})\}$ demonstrates the significant influence of epistemic uncertainties on the performance of primary structure. Therefore, it was necessary to perform the optimization that fully considered the influences of the epistemic uncertainty.

Given the mass ratios $\mu_T = 0.01,0.03$ and the design space of optimal parameters being set to $\omega_T \in [0,30]$, $\zeta_T \in [0,1]$, the optimal convergence histories were illustrated in Figures 5 and 6. In order to illustrate the suppressing effect of the TMD, the mitigation factor α_m was defined as follows:

$$\alpha_m = \mathrm{Exp}\{\bar{R}_{u_s u_s,T}(\boldsymbol{\theta},\boldsymbol{\eta})\}/\mathrm{Exp}\{\bar{R}_{u_s u_s,0}(\boldsymbol{\theta})\}, \tag{19}$$

where $\mathrm{Exp}\{\bar{R}_{u_s u_s,T}(\boldsymbol{\theta},\boldsymbol{\eta})\}$ and $\mathrm{Exp}\{\bar{R}_{u_s u_s,0}(\boldsymbol{\theta})\}$ denote the expectation of the UB of the evidential representation of the first-order statistical moment of the system response covariance with or without the TMD. As shown in Figures 5 and 6, the smaller value of α_m implied the excellent performance of the TMD. To elucidate the effectiveness of proposed method, the optimal results and contours of the mitigation ratio in the space design parameter were also plotted in Figures 5b and 6b.

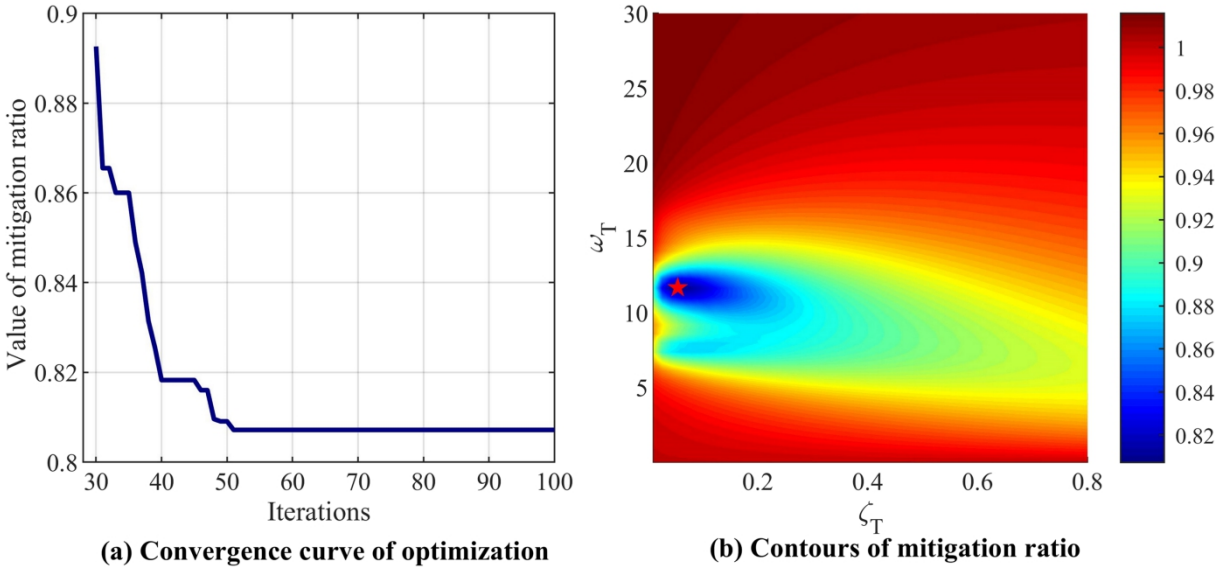

FIGURE 5 (a) Convergence history and (b) contours of the mitigation ratio with a mass ratio of $\mu_T = 0.01$

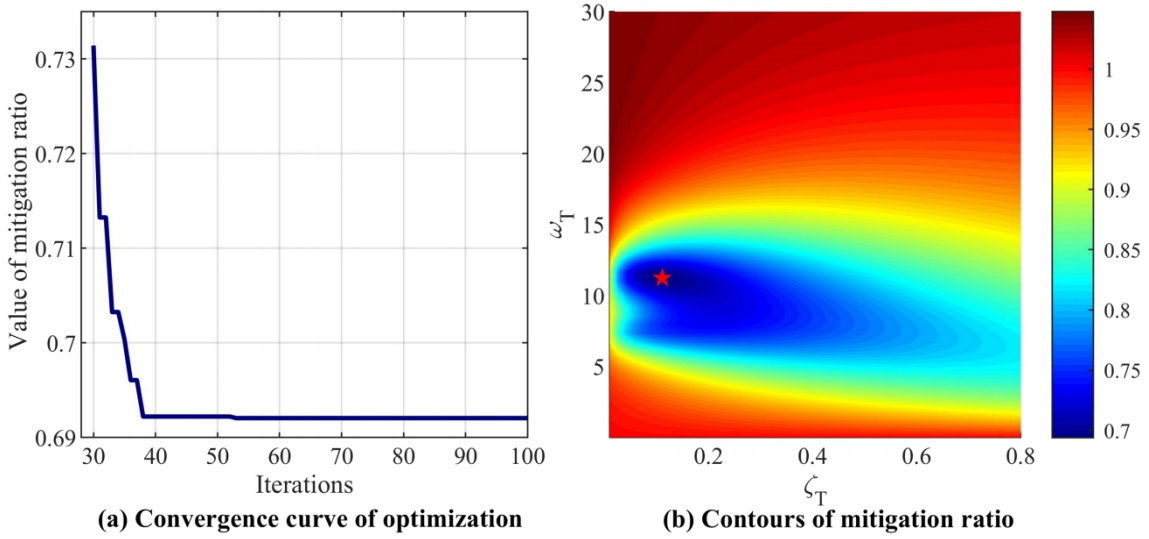

FIGURE 6 (a) Convergence history and (b) contours of the mitigation ratio with a mass ratio of $\mu_T = 0.03$

As indicated in Figures 5a and 6a, the optimal value close to the final optimal results for the iteration numbers that were less than 25 and 10. For the case of $\mu_T = 0.01$, the optimal value of $\mathrm{Exp}\{\bar{R}_{u_s u_s,T}(\boldsymbol{\theta},\boldsymbol{\eta})\}$ and the optimal parameters of ω_T and ζ_T were 0.0057, 11.67, and 0.054. The optimal parameters ω_T and ζ_T and the optimal value of $\mathrm{Exp}\{\bar{R}_{u_s u_s,T}(\boldsymbol{\theta},\boldsymbol{\eta})\}$ for the case of $\mu_T = 0.03$ were 11.32, 0.108, and 0.0049. Figures 5b and 6b show that the global optimal results occurred in the valley of the contour plots, which meant that the proposed two-loop optimization process could access the global optimal results.

Apart from searching the optimal parameters of the designed TMD for an SDOF system with specified nominal parameters, we also extended this procedure into general SDOF systems. The nominal value of structural period T_s ranges from 0.1 to 5 s, and the variation of dynamic system keeps constant. Given mass ratio $\mu_T = 0.03$ and 0.05, we got a series of optimal values of ω_T and ζ_T as shown in Figure 7. Additionally, we plotted the corresponding mitigation ratios to investigate the seismic performance of the designed TMD.

As shown in Figure 7a, the optimized frequency of TMD ω_T decreases with structural period. The well-matched curves of optimal ω_T for cases $\mu_T = 0.03$ and 0.05 illustrate that the tuned frequency of TMD mainly depends on the variation of structural period, which is compatible to the tuned characteristics of fixed-point theory. The fluctuation of damping ratio of TMD in Figure 7b may ascribe to the multi-global optimal value of the objective function. In addition to discuss the variation of designed parameters, Figure 7c indicates that the proposed method provides a robust optimal result regardless of the change of structural period. As shown in the above subsections, the proposed robust design method can efficiently suppress the system response of primary structure. In the next subsection, the investigation of the efficiency of the robust design of the TMD in the MDOF system is described.

5.2 | Optimal design of the TMD installed in the 10-story building

A 10-story shear building equipped with a single TMD is illustrated in Figure 8.[38] The mass ratio of the TMD was chosen with a prior value as 3% with respect to the total mass of the structure, and the optimal parameters were assumed to be the stiffness and damping coefficient of the TMD. The objective function $R_{d_{\max} d_{\max}}(\boldsymbol{\theta},\boldsymbol{\eta})$ of the optimal process was defined as the expectation of the maximum inter-story drift of the primary structure under the stationary excitation. For primary structure, the nominal values of the mass, stiffness, and damping coefficient were $m_i = 360 \times 10^3$ kg, $k_i = 650 \times 10^6$ N/m, and $c_i = 6.2 \times 10^6$ kN·s/m, $i = 1,2,...,10$. The uncertain information of these three parameters is summarized in Table 2. In optimal process, the LB and UB of the stiffness and damping coefficient of the TMD were set to 0–4000 kN/m and 0–1000 kN·s/m, respectively. The Kanai–Tajimi filter model was also employed in order to consider the site condition of the outside excitation. The nominal values of the Kanai–Tajimi filter model were set to $\omega_f = 37.3$ rad/s and $\zeta_f = 0.6$. The coefficients of variation of these three variables were set to 10%, and considering the scarcity of these data, the LB and UB were set to $\mu \pm 3\sigma$, where μ and σ denote the mean value and the standard deviation, respectively.

According to the uncertainty information listed in Table 2, the joint focal element of the uncertain system input was constructed by a Cartesian product $\boldsymbol{\theta}_q^{\mathrm{I}} = \left[(k_i)_{j_1}^{\mathrm{I}}, (m_i)_{j_2}^{\mathrm{I}} (c_i)_{j_3}^{\mathrm{I}}, (\omega_f)_{j_4}^{\mathrm{I}}, (\zeta_f)_{j_5}^{\mathrm{I}}, (S_0)_{j_6}^{\mathrm{I}}\right]^{\mathrm{T}}, j_i \in \forall[1,J_i], i \in [1,6], q \in [1,Q]$, where the number of joint focal elements was $Q = \prod_{i=1}^{6} J_i = 18$. Then the uncertainty propagation was implemented by using

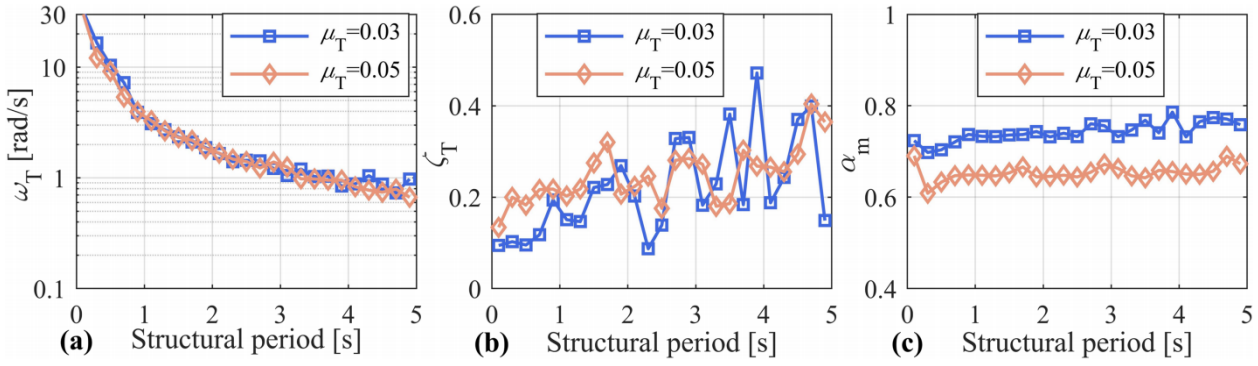

FIGURE 7 (a) Optimized ω_T, (b) optimized ζ_T, and (c) mitigation ratio with respect to structural period T_s

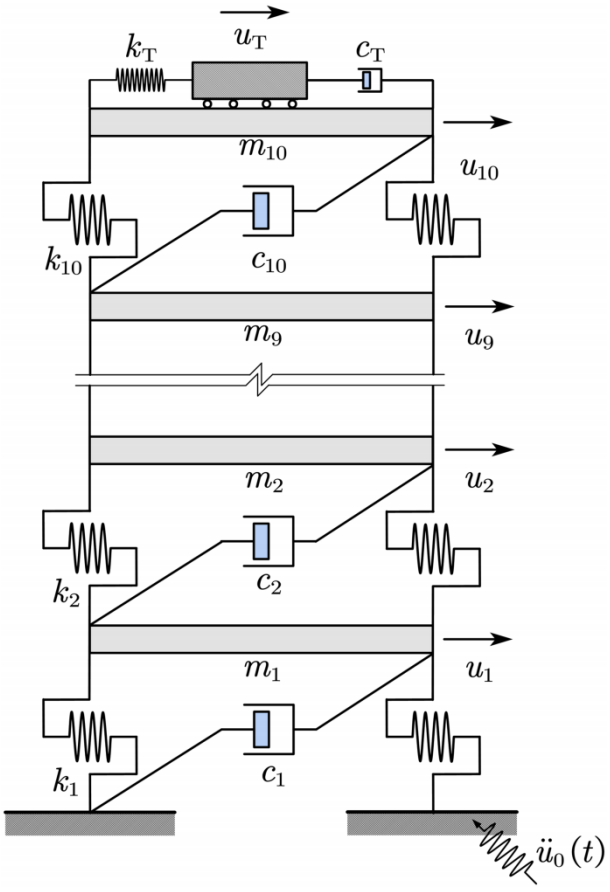

FIGURE 8 Schematic of the MDOF system equipped with a TMD

TABLE 2 Evidential representation of the uncertain parameters of the structural system and the site condition

k_i ($\times 10^6$ N/m)		m_i ($\times 10^3$ kg)		c_i ($\times 10^6$ N·s/m)		ω_f (rad/s)		ζ_f		S_0 (m^4/s^2)	
Focal element	**BBA**	**Focal element**	**BBA**	**Focal element**	**BBA**	**Focal element**	**BBA**	**Focal element**	**BBA**	**Focal element**	**BBA**
[358, 553]	0.165	[252, 324]	0.157	[5.58, 6.20]	0.5	[26.11, 48.49]	1	[0.51, 0.69]	1	[0.035, 0.065]	1
[553, 748]	0.683	[324, 396]	0.681	[6.20, 6.82]	0.5						
[748, 943]	0.153	[396, 468]	0.161								

the parallel-EGO algorithm. For this case, the number of initial DOE was determined to be 30, and the stop criterion was set to 100 calls to the performance function. The uncertainty propagation results for performance indicator without TMD $R_{d_{\max}d_{\max},0}(\boldsymbol{\theta})$ are plotted in Figure 9 with $\mathrm{CPF}_{\text{P-EGO}}$ and $\mathrm{CBF}_{\text{P-EGO}}$. The baseline results presented by the Monte Carlo simulation with 10^5 and 10^6 sampling and the corresponding uncertainty measure results are plotted in Figure 9. For these results, $\mathrm{CPF}_{\mathrm{MC}_1}$, $\mathrm{CPF}_{\mathrm{MC}_2}$, $\mathrm{CBF}_{\mathrm{MC}_1}$, and $\mathrm{CBF}_{\mathrm{MC}_2}$ were used to test the accuracy of the parallel-EGO-based results of the uncertainty propagation. A comparison of the uncertainty quantification results of performance indicator $R_{d_{\max}d_{\max},0}(\boldsymbol{\theta})$ was plotted in Figure 9 to elucidate the relationship between evidence theory framework and probabilistic model. In this case, the probabilistic models of structural parameters were assumed same with case study 1. Then, the probabilistic result represented with CDF in Figure 9 was obtained from the Monte Carlo simulation with 10^6 sampling.

As indicated in Figure 9, the Monte Carlo simulation results with 10^5 and 10^6 sampling may have provided a larger value for the CPF estimation and a smaller value for the CBF estimation of $R_{\mathrm{dd},0}(\boldsymbol{\theta})$. Meanwhile, the proposed parallel-EGO gave a wider distance for the CPF and CBF than the two Monte Carlo simulations did. For the performance

indicator $\mathrm{Exp}\{R_{d_{\max}d_{\max},0}(\boldsymbol{\theta})\}$, the uncertainty quantification results that were obtained using parallel-EGO and the Monte Carlo simulations with 10^5 and 10^6 samples were $[2.25\times10^{-4},0.0013]\times\mathrm{m}^2$, $[2.39\times10^{-4},0.0012]\times\mathrm{m}^2$, and $[2.46\times10^{-4},0.0012]\times\mathrm{m}^2$. Compared with the SDOF system, as described in first section, the influence of the epistemic uncertainty was enhanced with the increase of the number of degrees of freedom. In line with the previous case study for SDOF system, the CDF curve is employed to illustrate distribution of performance indicator under the influences of uncertain parameters with aleatory uncertainty. It is obviously found that the probabilistic model is in the gap between CBF and CPF curves. Furthermore, the comparison between probabilistic result and evidential results indicated that an overoptimistic model (e.g., probabilistic model) might lose the capacity to handle with the worst case denoted by the CBF and to keep the robustness of the design under the impact of epistemic uncertainties. Thus, a synthetic optimal framework of TMD that fully concerning the effect of epistemic uncertainty is significant to realize the robustness of seismic performance of designed TMD.

Given the mass ratio of $\mu_T = 0.03$ and the range of optimal parameters of $k_T \in [0,4000]$ kN/m and $c_T \in [0,1000]$ kN·s/m, the optimal convergence history is plotted in Figure 10. To validate the effectiveness of the proposed method, Figure 10b gives the contour plots and optimal value of the mitigation ratio in the space design.

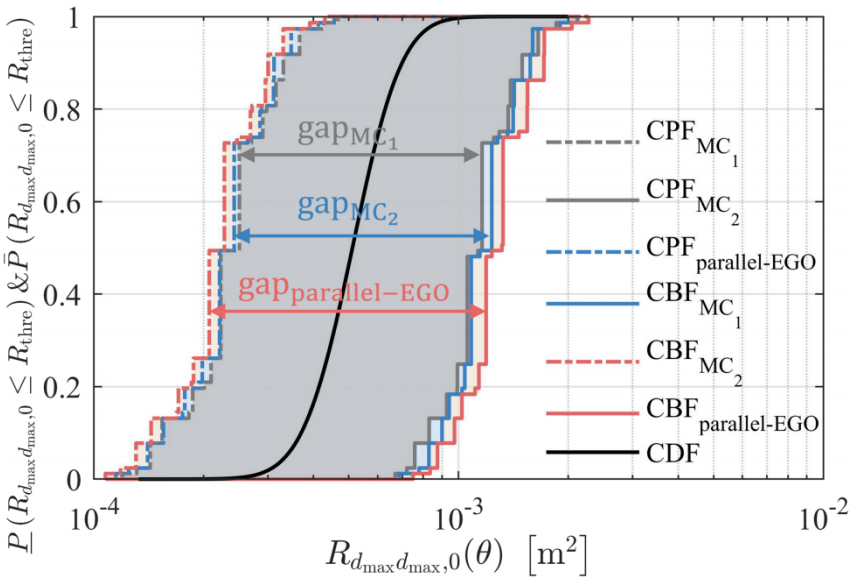

FIGURE 9 Comparison of the parallel-EGO results with the Monte Carlo simulations

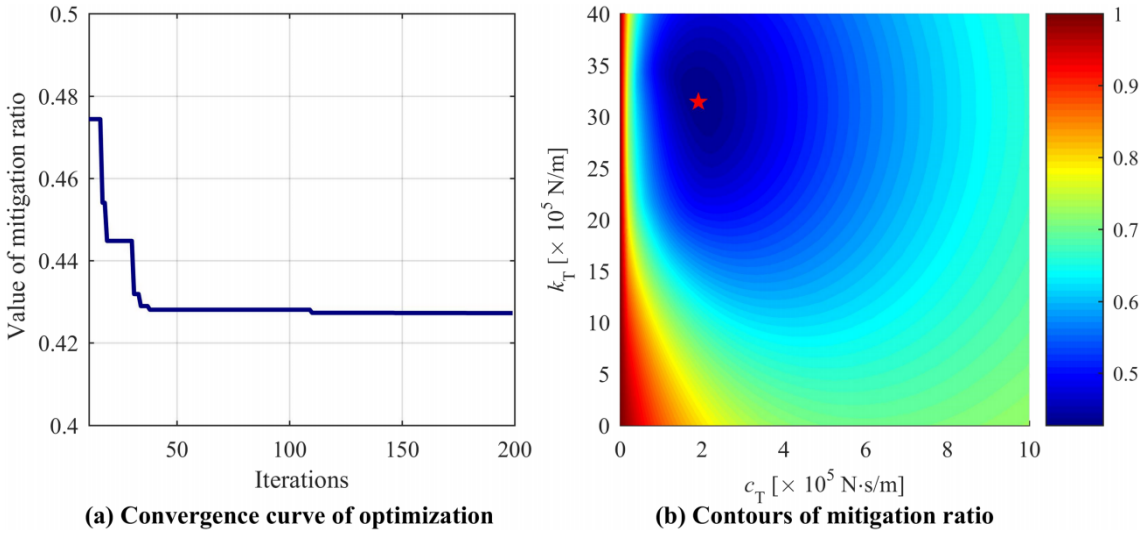

(a) Convergence curve of optimization (b) Contours of mitigation ratio

FIGURE 10 (a) Convergence history and (b) contour plot of the mitigation ratio with a mass ratio of $\mu_T = 0.03$

Figure 10a shows the initial value of the mitigation factor α_m of the inter-story drift hold of about 0.48, which was reduced quickly with the increment of iterations. The performance indicator stayed constant when the iteration number was larger than 120. The optimal parameters were as shown in Figure 10b, $k_T = 3143$ kN/m and $c_T = 191.5$ kN/m, the optimal value of the performance indicator was $\text{Exp}\{\bar{R}_{d_{\max}d_{\max},T}(\boldsymbol{\theta},\boldsymbol{\eta})\} = 5.55 \times 10^{-4}\,\text{m}^2$, and the relative mitigation factor was $\alpha_m = 0.427$. The location of the parameter combinations validated the effectiveness of the proposed method. It should be noted that for the traditional optimization method based on the "fixed point," the optimal results should have been consistent with the fundamental frequency of the structure. However, the stochastic vibration method controlled the vibration using the integral in the frequency domain, which led to a global control effect. To validate the seismic performance of designed TMD, a series of the time history analysis was conducted.

5.3 | Time history validation for the optimal results with the selected ground motions

In this part, four ground motions consist of the general ground motions (El Centro and Taft) and near-fault ground motions with long-period pulse (Kobe and Chi-Chi). In order to illustrate the reduction of the designed TMD with a fair way and avoid the influences of intensity of ground motions, the peak ground accelerations (PGAs) of four ground motions were rescaled to 300 gal. The absolute acceleration response spectrums of the scaled ground motions were reported in Figure 11. In order to illuminate the seismic performance of designed TMD under ground motion excitations, we also plot the LB and UB of the expectation of fundamental period of the primary structure as gray bond in Figure 11.

Because the aleatory and epistemic uncertainties were involved in the structural system and external excitation, the time history validation was separated as two aspects, one was to investigate structural responses with nominal value and the other was to explore the structural responses that with uncertainties. The root-mean-square (RMS) values and MAX values of roof displacement u_{10}, ninth absolute acceleration $\ddot{u}_{9,0}$, and fifth inter-story drift d_5 of primary structure were employed to explore the seismic performance of the designed TMD. Meanwhile, a reduction factor with negative percentages was used to approximate the mitigation of the designed TMD compared to the original structural system.

5.3.1 | Validation of mitigation effect of the designed TMD with deterministic parameters

In the first scenario, the nominal values of structural parameters were employed to estimate the system responses subject to the selected ground motions. The RMS values of the performance indicators were reported in Table 3.

As reported in Table 3, the mitigation percentages of the roof displacement u_{10} are from 26% to 40%, and ninth absolute acceleration is from 22% to 36% for the selected ground motions. The similar reductions of fifth inter-story drift were observed in Table 3. Table 3 implies that the installation of the designed TMD leads to an excellent mitigation for the RMS values of primary structure. Furthermore, the comparison of time history of the system responses u_{10}, $\ddot{u}_{9,0}$, and d_5 of primary structure subjected to the El Centro and Chi-Chi waves were listed in Figure 12.

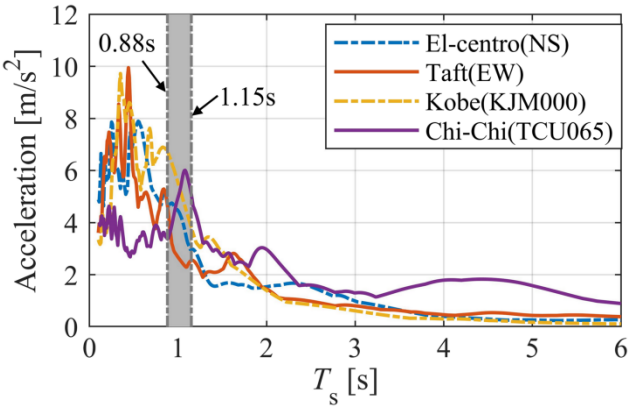

FIGURE 11 Response spectrum of the selected ground motions

TABLE 3 List of RMS value of system response of MDOF system attached with the designed TMD

Events	u_{10} (mm)	$\ddot{u}_{9,0}$ (m/s^2)	d_5 (mm)
El Centro	21.6 (−31%)	0.90 (−29%)	2.2 (−31%)
Taft	19.2 (−26%)	0.87 (−22%)	2.0 (−25%)
Kobe	23.2 (−40%)	1.00 (−36%)	2.4 (−39%)
Chi-Chi	20.5 (−26%)	0.79 (−27%)	2.1 (−26%)

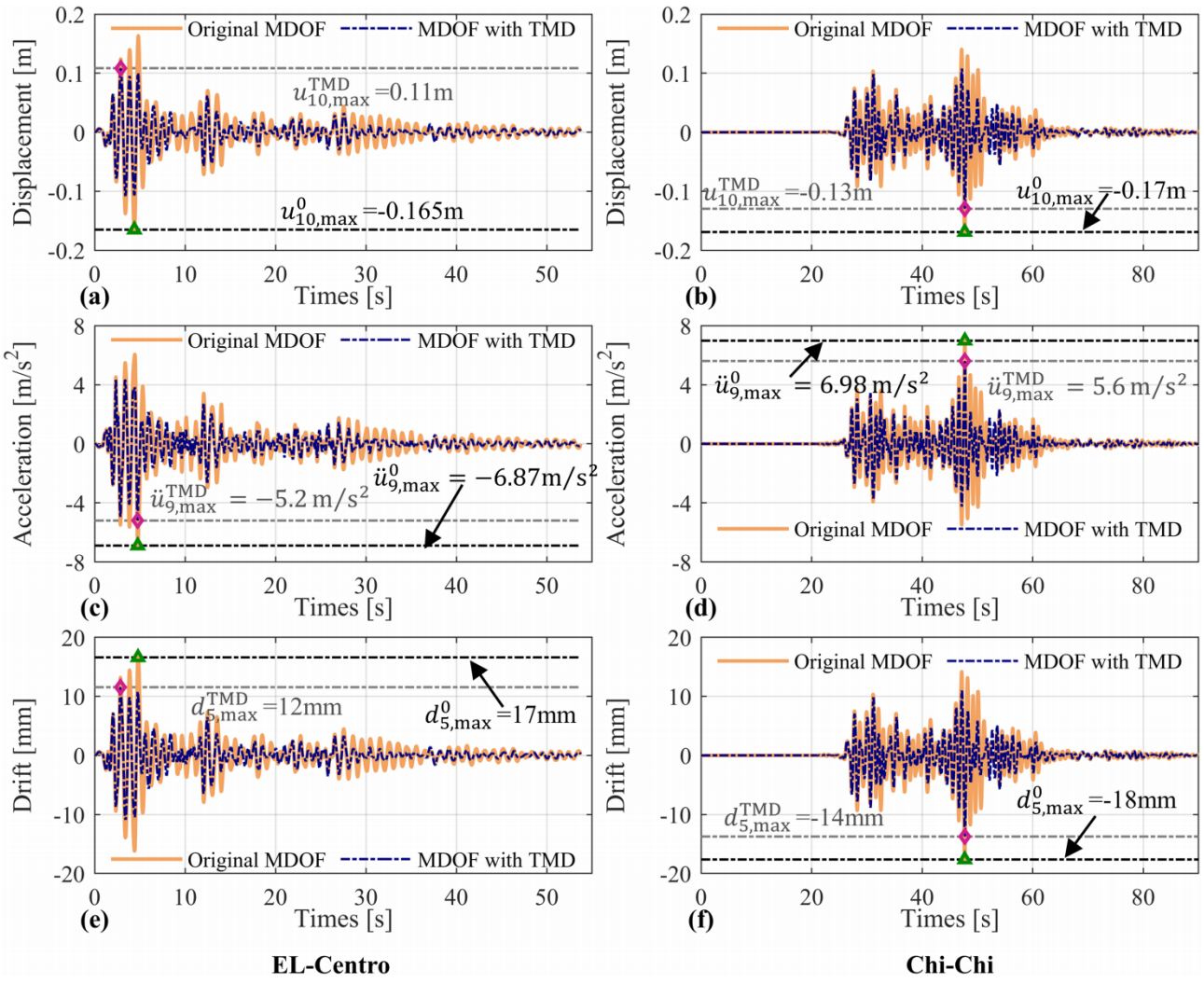

FIGURE 12 Time history of the (a, b) roof displacement, (c, d) ninth absolute acceleration responses, and (e, f) fifth inter-story drift of MDOF system

As illustrated in Figure 12a–f, the time histories of performance indicators reduce obviously by equipping the designed TMD. It emerges that the MAX value of u_{10} reduces from 0.0165 to 0.011 m and related reduction factor was almost −33% under the El Centro ground motion. Moreover, the absolute acceleration $\ddot{u}_{9,0}$ achieves an excellent reduction, and the related reduction factors were −24% and −20% for cases of El Centro and Chi-Chi ground motions. The mitigation of d_5 is also manifested in Figure 12e,f. To date, the time history investigation manifests the excellent performance of the designed TMD for MDOF system with nominal values.

TABLE 4 List of the UBs of the RMS values of the system responses

Events	$\bar{\sigma}_{u_{10}}$ (mm)	$\bar{\sigma}_{\ddot{u}_{9,0}}$ (m/s^2)	$\bar{\sigma}_{d_5}$ (mm)
El Centro	24.9 (−39%)	1.29 (−37%)	2.6 (−39%)
Taft	23.0 (−36%)	1.24 (−32%)	2.4 (−35%)
Kobe	25.5 (−44%)	1.35 (−29%)	2.7 (−43%)
Chi-Chi	30.6 (−51%)	0.93 (−56%)	3.1 (−51%)

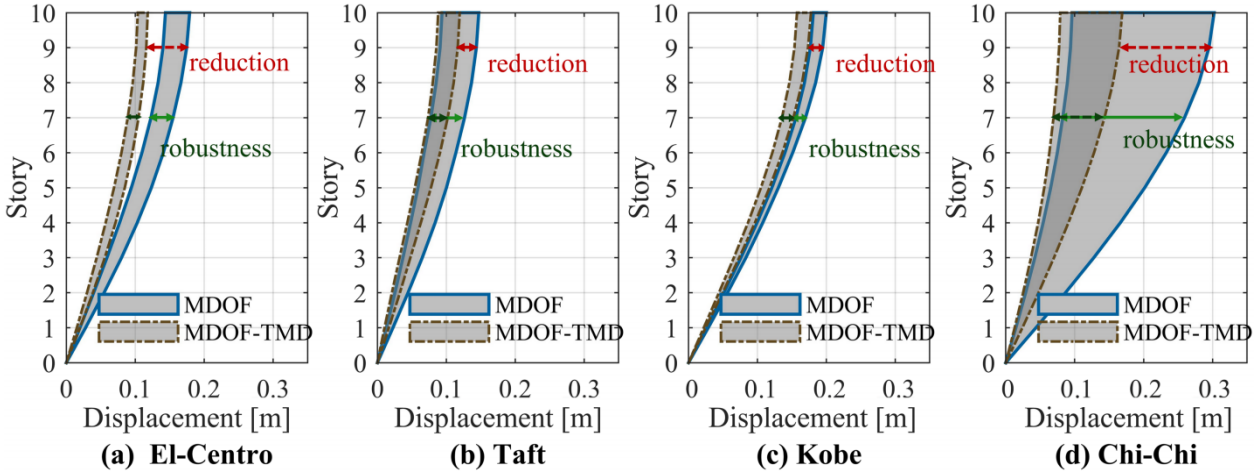

FIGURE 13 MAX values of the displacement responses of MDOF system

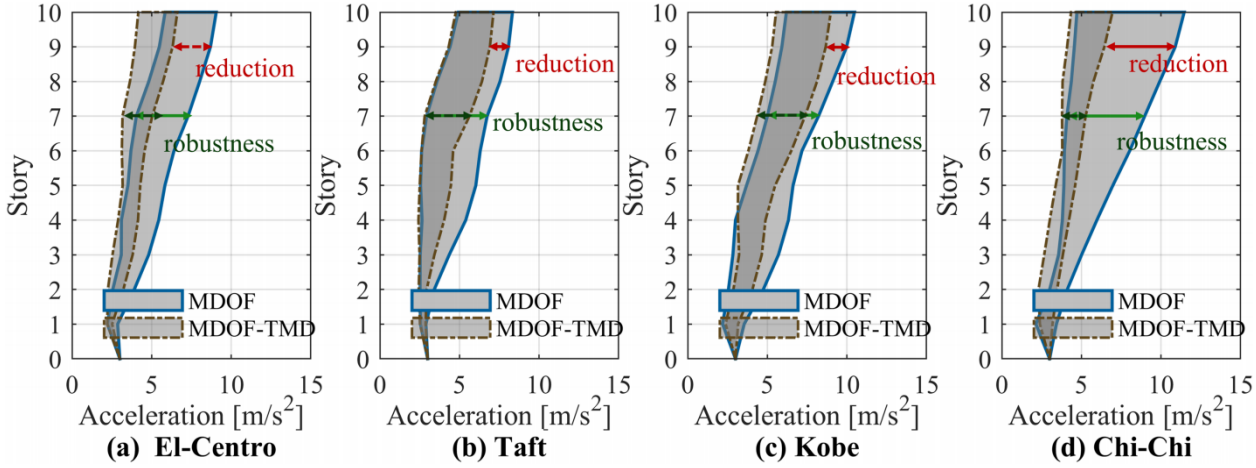

FIGURE 14 MAX values of the absolute acceleration responses of MDOF system

5.3.2 | Seismic performance validation of the designed TMD with uncertain parameters

In this part, the seismic performance of the designed TMD was explored by considering the uncertainties rooted in the primary structures. Because the epistemic uncertainties were represented by the discrete intervals as mentioned above, the mitigation of the designed TMD shall be divided as two aspects. On the one hand, the reduction of the worst case of system responses should be investigated, which is expressed as the reduction of UB of system responses. On the other hand, the enhancement of robustness of structural system also needs to be investigated, because the robustness of control effect reflects the capability of TMD for the extreme condition. Generally speaking, the robustness of system response can be expressed as the gap between the LB and UB of system responses. To illustrate the control effect of the

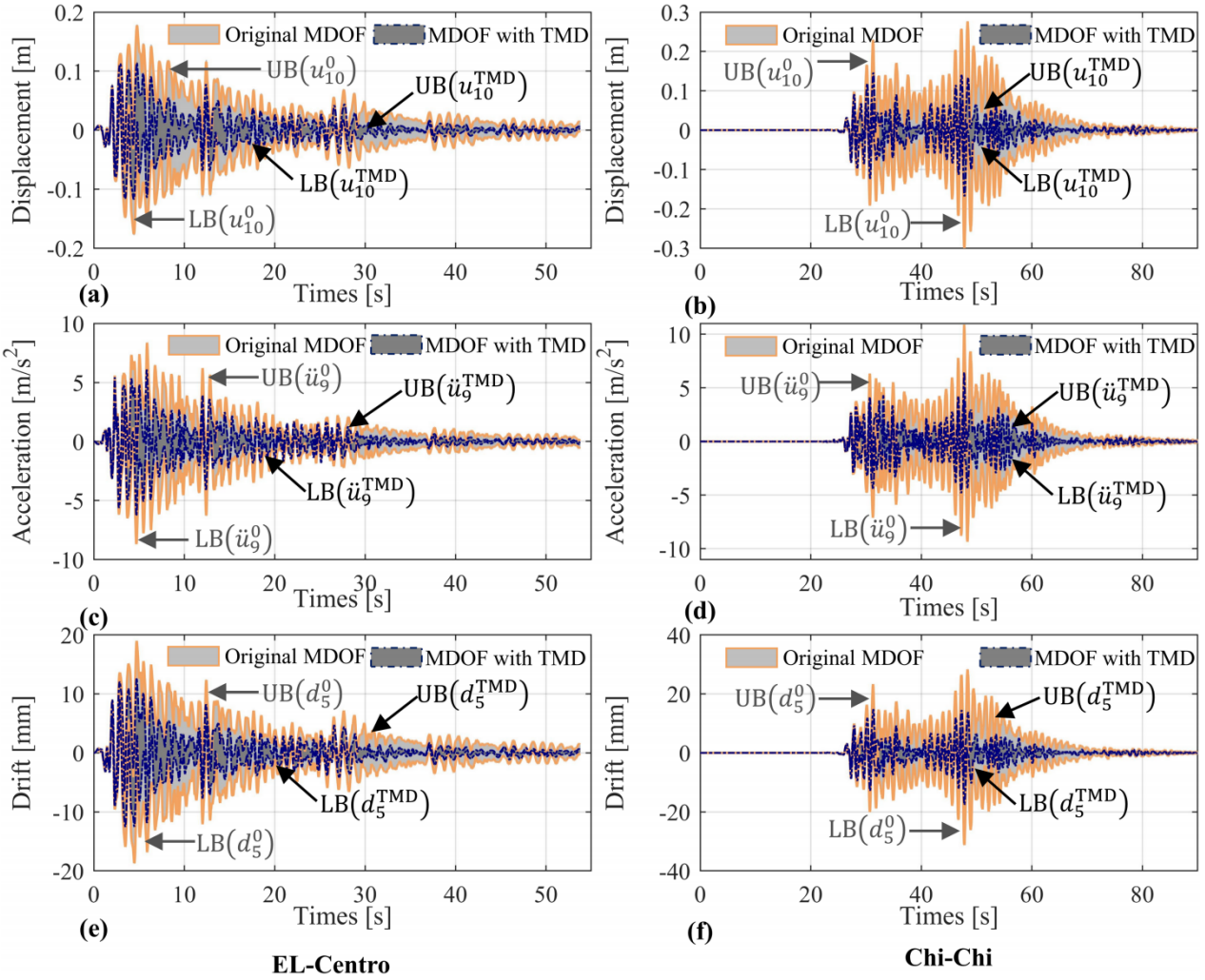

FIGURE 15 Time history of the (a, b) displacement responses, (c, d) the ninth absolute acceleration responses, and (e, f) the fifth inter-story drift of MDOF system

designed TMD, we compared the UBs and LBs of the performance indicators as noted above. The joint focal element with respect to the k_i, c_i, and m_i [553,748] $\times$ 10^6 N/m, [324,396] $\times$ 10^3 kg, and [5.58,6.2] $\times$ 10^6 N·s/m were selected to conduct the time history analysis. A Latin hypercube design with 1000 samples was employed to evaluate the UBs and LBs of system responses. As defined in Equation (19), the mitigation for MDOF system attaching with the designed TMD subjected to the selected ground motions was reported in Table 4.

Table 4 illustrates that the designed TMD results in an excellent release of the UB of performance indicator, where the reduction of the UB of RMS value of u_{10} was as much as 51% under Chi-Chi wave. Moreover, the reductions of the UB of RMS value of $\ddot{u}_{9,0}$ and d_5 calculated from the El Centro and Taft excitations were 37%, 32% and 39%, 35%, respectively. It is interesting to observe that the designed TMD achieves a better performance for Kobe and Chi-Chi ground motions than the other two ground motions. That can be explained by using Figure 11. Because the expectation interval of fundamental period of the primary structure ranges from 0.88 to 1.15 s, the designed TMD can perform excellently in this interval due to the tuned mechanics. Furthermore, we found that the response spectrum of Kobe and Chi-Chi ground motions yields a higher value in this period interval. Therefore, the designed TMD can achieve a significant reduction for these two ground motions. In order to manifest the mitigation effect of designed TMD with a comprehensive way, we also compared the interval formed MAX values of the performance indicators. The comparisons of the MAX values of the displacement responses and absolute acceleration responses of the primary structure with or without the designed TMD were depicted in Figures 13 and 14.

As illustrated in Figures 13 and 14, the MAX values of the displacement responses and absolute acceleration responses of primary structure were represented by the intervals. It is worthy to note that the gaps between the UBs

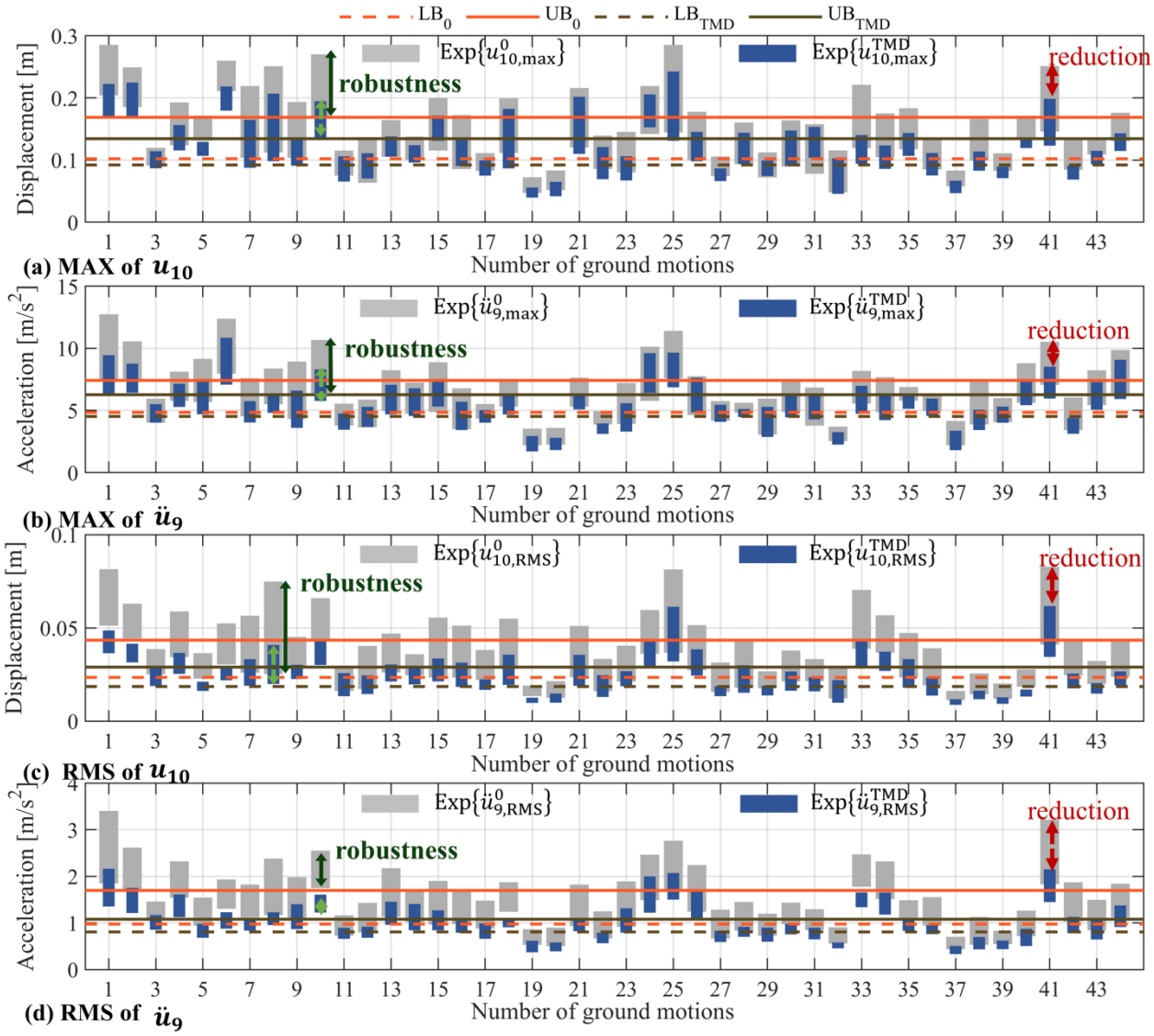

FIGURE 16 Comparisons of seismic performance indicators: (a) MAX value of the roof displacement $\boldsymbol{u_{10}}$, (b) MAX value of the ninth absolute acceleration $\boldsymbol{\ddot{u}_9}$, (c) RMS value of the roof displacement $\boldsymbol{u_{10}}$, and (d) RMS value of the ninth absolute acceleration $\boldsymbol{\ddot{u}_9}$ under 44 records of far-field ground motions

and LBs of system responses plotted in Figures 13 and 14 were reduced significantly by equipping the designed TMD. Therefore, we can conclude that the system robustness of primary MDOF system was improved remarkably by attaching the designed TMD. Additionally, we compared the LBs and UBs of the structural responses u_{10}, $\ddot{u}_{9,0}$, and d_5 of MDOF system subjected to El Centro and Taft ground motions in Figure 15.

As depicted in Figure 15, the roof displacement, ninth absolute acceleration, and fifth inter-story drift were reduced in the whole-time range. The intervals of performance indicators with the time steps highlight that the designed TMD by considering the epistemic uncertainties keeps effectiveness and efficacy subjected to the natural ground motions.

5.4 | Time history validation for the optimal results with the selected ground motion set

A set of ground motions that consists of 44 records of the far-field ground motions and 28 records of the near-field ground motions with strong pulse was selected from the FEMA P-695 report[59,60] to test the seismic performance of the designed TMD. The MAX value and RMS value of expectation of roof displacement u_{10} and ninth absolute acceleration

$\ddot{u}_9$ were used to illustrate the improvement of seismic performance of MDOF system by installing the designed TMD. Figure 16 collects four performance indicators of primary structure under the selected far-field excitations. Furthermore, the median values of the LBs and UBs of the performance indicators were indicated with dash line and solid line, respectively.

As shown in Figure 16, the installation of the designed TMD results in an excellent reduction for the selected performance indicators of the primary structure. For performance indicator u_{10}, the installation of designed TMD yields a reduction of the MAX value and RMS value from 2% to 36% and from 12% to 45%, respectively. Meanwhile, the reduction of the MAX value and RMS value of $\ddot{u}_9$ achieves from 2% to 33% and from 18% to 48%, respectively. Additionally, Figure 16 shows that the reduction of median value of four performance indicators is 20%, 16%, 33%, and 36%, respectively. Therefore, results shown in Figure 16 indicate that, as expected, the reductions of worst cases and the improvements of robustness of performance indicators are achieved simultaneously. Apart from the investigation of seismic performance designed TMD under the far-field ground motions, Figure 17 gives a collection of the performance indicators of primary structure subjected to the near-field ground motions with strong pulse.

Figure 17 shows that the performance indicator of primary structure significantly reduced by installing the designed TMD. The reduction of median of performance indicators yields 13%, 13%, 33%, and 37%. It is worthy to note that the

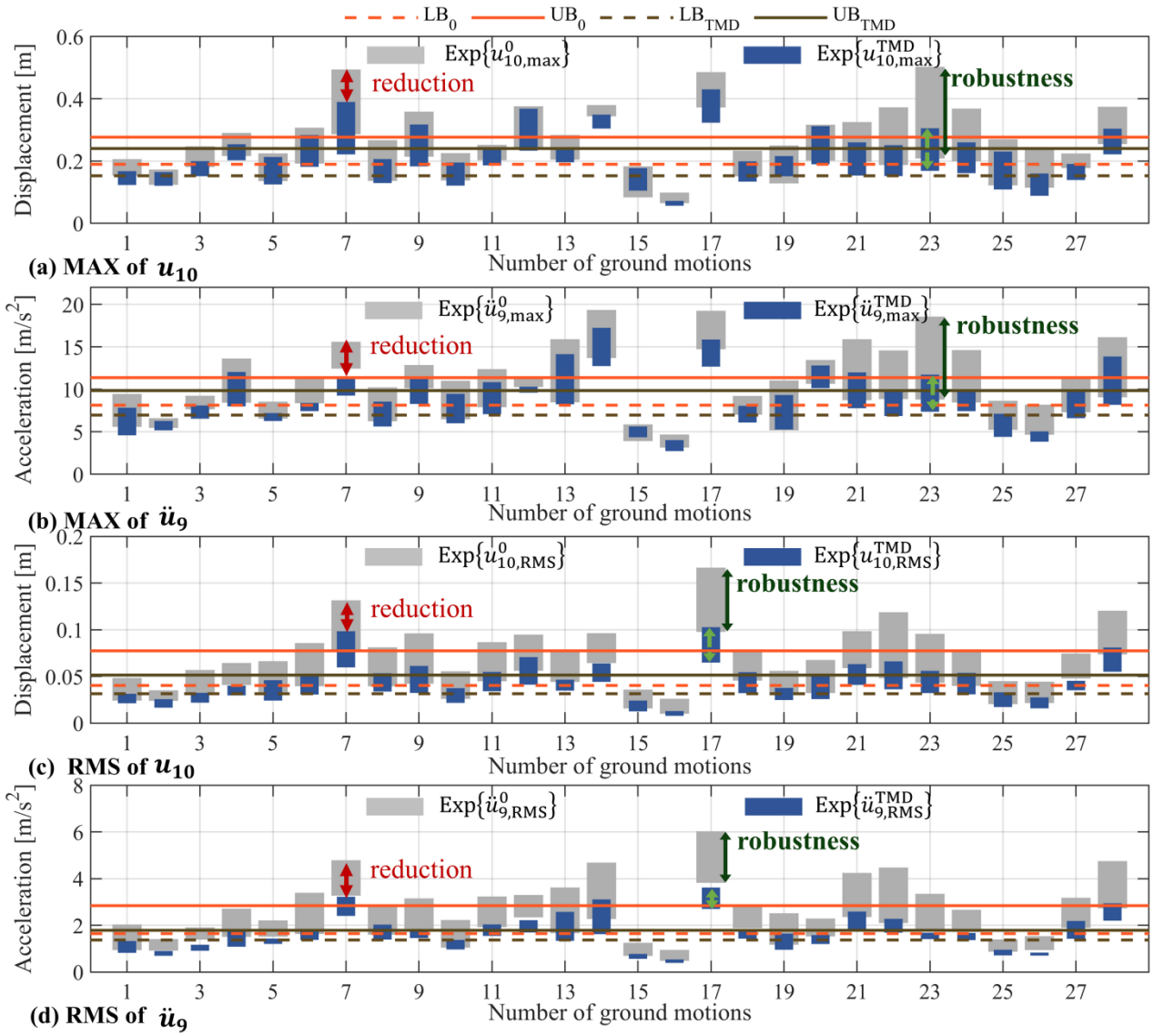

FIGURE 17 Comparisons of seismic performance indicators: (a) MAX value of the roof displacement $\boldsymbol{u_{10}}$, (b) MAX value of the ninth absolute acceleration $\boldsymbol{\ddot{u}_9}$, (c) RMS value of the roof displacement $\boldsymbol{u_{10}}$, and (d) RMS value of the ninth absolute acceleration $\boldsymbol{\ddot{u}_9}$ under 28 records of near-field ground motions with strong pulse

amplitudes of the LB and UB of median performance indicators are considerably reduced as shown in Figures 16 and 17. That is used to validate the improvement of robustness of primary structure with the designed TMD. To summarize above, the designed TMD not only can reduce the worst cases but also can improve the robustness for the structural responses that include the effect of epistemic uncertainties.

6 | CONCLUSIONS

The main contribution of this work is to propose a robust design method for a TMD with consideration of the hybrid uncertainties rooted in the external excitation, site conditions, and structural model. In this method, the aleatory uncertainty of external excitation was expressed with white noise, and the epistemic uncertainty related to incomplete knowledge of the parameters of site conditions and primary structure was well modeled with the evidence theory. The proposed parallel-EGO effectively releases the computational burden of the uncertainty propagation with evidence theory. By precisely approximating the UB of the first-order statistical moment of system responses, a robust design framework for a TMD was presented in Section 4.

The case studies for an SDOF system and MDOF system equipped with the designed TMD highlight the following characteristics for the proposed method:

- The proposed parallel-EGO holds a higher precision than the Monte Carlo simulations with 10^6 samples in evidential uncertainty propagation. On the other hand, the computational burden for the robust design of a TMD with considering aleatory and epistemic uncertainties was drastically alleviated by employing the parallel-EGO.
- The fast convergence history and contour plot of the mitigation factor α_{m} as reported in Section 5 shows that the proposed robust design framework can capture the global optimum set exactly.
- The time history analysis results in Sections 5.3 and 5.4 proves that the designed TMD can mitigate the worst system responses and improve the robustness of primary structure, simultaneously.

To the end, the robust design method presented in this study ensures the efficacy and effectiveness of the designed TMD. The further step for research work will aim to expanding the study to the life cycle cost of the passive control devices.

ACKNOWLEDGMENTS

This study was supported by the Ministry of Science and Technology of the People's Republic of China (Grant No. SLDRCE19-B-02), the National Basic Research Program of China (973 Program) (Grant No. 2017YFC0703607), the Natural Science Foundation of Shanghai (Grant No. 17ZR1431900), and the National Natural Science Foundation of China (Grant No. 51178337).

AUTHOR CONTRIBUTIONS

Dawei Li: methodology; software; formal analysis; writing—original draft; validation; visualization; writing—review and editing. **Hesheng Tang**: funding acquisition; investigation; writing—original draft; writing—review and editing. **Songtao Xue**: funding acquisition; methodology; supervision; writing—review and editing.

NOMENCLATURE

$\ddot{\boldsymbol{u}}_{\mathbf{g}}$	acceleration of the external excitation
$\ddot{\boldsymbol{u}}_{\mathbf{w}}$	acceleration of the stationary Gaussian white noise
$\mathbf{M_s}$, $\mathbf{C_s}$, $\mathbf{K_s}$	mass, damping coefficient, and stiffness matrixes of the primary structure
$\mathbf{R}_{YY}$, $\mathbf{R}_{ZZ}$	covariance matrix of the state vector and observation vector
$\boldsymbol{S}_{\mathbf{0}}$	intensity of a two-sided power spectral density function
$\boldsymbol{c}_{\mathbf{T}}$	damping coefficient of the TMD
$\boldsymbol{k}_{\mathbf{T}}$	stiffness of the TMD
$\boldsymbol{m}_{\mathbf{T}}$	mass of the TMD
$\boldsymbol{u}_{\mathbf{T}}$	displacement response of the TMD
$\boldsymbol{u}_{\mathbf{s}}, \dot{\boldsymbol{u}}_{\mathbf{s}}, \ddot{\boldsymbol{u}}_{\mathbf{s}}$	vectors for displacement, velocity, and acceleration of the primary structure
$\boldsymbol{\alpha}_{\mathbf{m}}$	mitigation factor of the structural response

ζ_f	efficient damping ratio related to the Kanai–Tajimi model
μ_T	mass ratio of the TMD
ω_f	dominant frequency related to the Kanai–Tajimi model
$\mathbf{A}$, $\boldsymbol{B}$	state space matrix and input vector of structural system
$\boldsymbol{b}$	location vector of damping and stiffness of the TMD
$\mathbf{M}$, $\mathbf{C}$, $\mathbf{K}$	mass, damping coefficient, and stiffness matrixes of structural system equipped with TMD
$\boldsymbol{Y}$, $\boldsymbol{Z}$	state vector and observation vector of the state space equation
$\boldsymbol{a}$	location vector of mass of the TMD
$\boldsymbol{f}$	external excitation of the structural system
$\boldsymbol{u}$, $\dot{\boldsymbol{u}}$, $\ddot{\boldsymbol{u}}$	vectors for displacement, velocity, and acceleration of structural system equipped with TMD
$\boldsymbol{\Gamma}$	output selection matrix of the state space equation
$\boldsymbol{\alpha}$	$N \times 1$ independent variable related to the structural system
$\boldsymbol{\beta}$	$L \times 1$ independent variable related to the external excitation
$\boldsymbol{\eta}$	design vector related to robust design
$\boldsymbol{\theta}$	$(N+L) \times 1$ complete uncertain vector

ORCID

Hesheng Tang https://orcid.org/0000-0002-4241-6026

REFERENCES

1. Nishitani A, Inoue Y. Overview of the application of active/semiactive control to building structures in Japan. *Earthq Eng Struct Dyn*. 2001;30(11):1565-1574. https://doi.org/10.1002/eqe.81
2. Gutierrez Soto M, Adeli H. Tuned mass dampers. *Arch Comput Meth Eng*. 2013;20(4):419-431. https://doi.org/10.1007/s11831-013-9091-7
3. Sun JQ, Jolly MR, Norris MA. Passive, adaptive and active tuned vibration absorbers—a survey. *J Mech Des*. 1995;117(B):234-242. https://doi.org/10.1115/1.2836462
4. Elias S, Matsagar V. Research developments in vibration control of structures using passive tuned mass dampers. *Annu Rev Control*. 2017;44:129-156. https://doi.org/10.1016/j.arcontrol.2017.09.015
5. Kiani M, Vaseghi Amiri J. Effects of hysteretic damping on the seismic performance of tuned mass dampers. *Struct Design Tall Spec Build*. 2019;28(1):1-16, e1555. https://doi.org/10.1002/tal.1555
6. Boccamazzo A, Biagio C, Quaranta G, Lacarbonara W. Seismic effectiveness of hysteretic tuned mass dampers for inelastic structures. *Eng Struct*. 2020;216:1-14, 110591. https://doi.org/10.1016/j.engstruct.2020.110591
7. Venanzi I, Materazzi AL. Robust optimization of a hybrid control system for wind-exposed tall buildings with uncertain mass distribution. *Smart Struct Syst*. 2013;12(6):641-659. https://doi.org/10.12989/SSS.2013.12.6.641
8. Sun C, Nagarajaiah S. Study on semi-active tuned mass damper with variable damping and stiffness under seismic excitations. *Struct Control Health Monit*. 2014;21(6):890-906. https://doi.org/10.1002/stc.1620
9. Li C, Cao B. Hybrid active tuned mass dampers for structures under the ground acceleration. *Struct Control Health Monit*. 2015;22(4):757-773. https://doi.org/10.1002/stc.1716
10. Elias S, Matsagar V, Datta TK. Effectiveness of distributed tuned mass dampers for multi-mode control of chimney under earthquakes. *Eng Struct*. 2016;124:1-16. https://doi.org/10.1016/j.engstruct.2016.06.006
11. Gill D, Elias S, Steinbrecher A, Schröder C, Matsagar V. Robustness of multi-mode control using tuned mass dampers for seismically excited structures. *Bull Earthq Eng*. 2017;15(12):5579-5603. https://doi.org/10.1007/s10518-017-0187-6
12. Den Hartog JP. *Mechanical Vibrations*. New York: Courier Corporation; 1985.
13. Lee CL, Chen YT, Chung LL, Wang YP. Optimal design theories and applications of tuned mass dampers. *Eng Struct*. 2006;28(1):43-53. https://doi.org/10.1016/j.engstruct.2005.06.023
14. Chang CM, Shia S, Lai YA. Seismic design of passive tuned mass damper parameters using active control algorithm. *J Sound Vib*. 2018;426:150-165. https://doi.org/10.1016/j.jsv.2018.04.017
15. Warburton GB, Ayorinde EO. Optimum absorber parameters for simple systems. *Earthq Eng Struct Dyn*. 1980;8(3):197-217. https://doi.org/10.1002/eqe.4290080302
16. Liu K, Liu J. The damped dynamic vibration absorbers: revisited and new result. *J Sound Vib*. 2005;284(3–5):1181-1189. https://doi.org/10.1016/j.jsv.2004.08.002
17. Bakre SV, Jangid RS. Optimum parameters of tuned mass damper for damped main system. *Struct Control Health Monit*. 2007;14(3):448-470. https://doi.org/10.1002/stc.166
18. Ghosh A, Basu B. A closed-form optimal tuning criterion for TMD in damped structures. *Struct Control Health Monit*. 2007;14(4):681-692. https://doi.org/10.1002/stc.176
19. Bekdaş G, Nigdeli SM. Mass ratio factor for optimum tuned mass damper strategies. *Int J Mech Sci*. 2013;71:68-84. https://doi.org/10.1016/j.ijmecsci.2013.03.014

20. Leung AYT, Zhang H. Particle swarm optimization of tuned mass dampers. *Eng Struct*. 2009;31(3):715-728. https://doi.org/10.1016/j.engstruct.2008.11.017
21. Özsarıyıldız ŞS, Bozer A. Finding optimal parameters of tuned mass dampers. *Struct Design Tall Spec Build*. 2015;24(6):461-475. https://doi.org/10.1002/tal.1174
22. Yazdi H, Saberi H, Saberi H, Hatami F. Designing optimal tuned mass dampers using improved harmony search algorithm. *Adv Struct Eng*. 2016;19(10):1620-1636. https://doi.org/10.1177/1369433216646018
23. Igusa T, Der Kiureghian A. Response of uncertain systems to stochastic excitation. *J Eng Mech*. 1988;114(5):812-832. https://doi.org/10.1061/(ASCE)0733-9399(1988)114:5(812)
24. Iwan WD, Jensen H. Response of systems with uncertain parameters to stochastic excitation. *J Eng Mech*. 1992; 118(12):3285-3296. https://doi.org/10.1061/(ASCE)0733-9399(1992)118:5(1012)
25. Zang C, Friswell MI, Mottershead JE. A review of robust optimal design and its application in dynamics. *Comput Struct*. 2005;83(4–5):315-326. https://doi.org/10.1016/j.compstruc.2004.10.007
26. Marano GC, Greco R, Sgobba S. A comparison between different robust optimum design approaches: application to tuned mass dampers. *Prob Eng Mech*. 2010;25(1):108-118. https://doi.org/10.1016/j.probengmech.2009.08.004
27. Jensen H, Setareh M, Peek R. TMDs for vibration control of systems with uncertain properties. *J Struct Eng*. 1992;118(12):3285-3296. https://doi.org/10.1061/(ASCE)0733-9445(1992)118:12(3285)
28. Yu H, Gillot F, Ichchou M. Reliability based robust design optimization for tuned mass damper in passive vibration control of deterministic/uncertain structures. *J Sound Vib*. 2013;332(9):2222-2238. https://doi.org/10.1016/j.jsv.2012.12.014
29. Greco R, Marano GC. Optimum design of Tuned Mass Dampers by displacement and energy perspectives. *Soil Dyn Earthq Eng*. 2013;49:243-253. https://doi.org/10.1016/j.soildyn.2013.02.013
30. Greco R, Lucchini A, Marano GC. Robust design of tuned mass dampers installed on multi-degree-of-freedom structures subjected to seismic action. *Eng Optim*. 2015;47(8):1009-1030. https://doi.org/10.1080/0305215X.2014.941288
31. Venanzi I. Robust optimal design of tuned mass dampers for tall buildings with uncertain parameters. *Struct Multidiscip Optim*. 2015;51(1):239-250. https://doi.org/10.1007/s00158-014-1129-4
32. Rathi AK, Chakraborty A. Reliability-based performance optimization of TMD for vibration control of structures with uncertainty in parameters and excitation. *Struct Control Health Monit*. 2017;24(1):1-19, e1857. https://doi.org/10.1002/stc.1857
33. Bhattacharjya S, Chakraborty S. Robust optimization of structures subjected to stochastic earthquake with limited information on system parameter uncertainty. *Eng Optim*. 2011;43(12):1311-1330. https://doi.org/10.1080/0305215X.2011.554545
34. Chakraborty S, Roy BK. Reliability based optimum design of Tuned Mass Damper in seismic vibration control of structures with bounded uncertain parameters. *Prob Eng Mech*. 2011;26(2):215-221. https://doi.org/10.1016/j.probengmech.2010.07.007
35. Schmelzer B, Oberguggenberger M, Adam C. Efficiency of tuned mass dampers with uncertain parameters on the performance of structures under stochastic excitation. *Proc Inst Mech Eng Part O: J Risk Reliab*. 2010;224(4):297-308. https://doi.org/10.1243/1748006XJRR310
36. Adam C, Oberguggenberger M, Schmelzer B. Seismic performance of tuned mass dampers with uncertain parameters. In: Hofstetter G, ed. *Computational Engineering*. Cham: Springer International Publishing; 2014.
37. Marano GC, Quaranta G. Robust optimum criteria for tuned mass dampers in fuzzy environments. *Appl Soft Comput*. 2009;9(4):1232-1243. https://doi.org/10.1016/j.asoc.2009.03.010
38. Mrabet E, Guedri M, Ichchou MN, Ghanmi S. Stochastic structural and reliability based optimization of tuned mass damper. *Mech Syst Signal Process*. 2015;60–61:437-451. https://doi.org/10.1016/j.ymssp.2015.02.014
39. Mrabet E, Guedri M, Ichchou M, Ghanmi S. New approaches in reliability based optimization of tuned mass damper in presence of uncertain bounded parameters. *J Sound Vib*. 2015;355:93-116. https://doi.org/10.1016/j.jsv.2015.06.009
40. Lievens K, Lombaert G, De Roeck G, Van den Broeck P. Robust design of a TMD for the vibration serviceability of a footbridge. *Eng Struct*. 2016;123:408-418. https://doi.org/10.1016/j.engstruct.2016.05.028
41. Beer M, Ferson S, Kreinovich V. Imprecise probabilities in engineering analyses. *Mech Syst Signal Process*. 2013;37(1–2):4-29. https://doi.org/10.1016/j.ymssp.2013.01.024
42. Schöbi R, Sudret B. Structural reliability analysis for p-boxes using multi-level meta-models. *Prob Eng Mech*. 2017;48:27-38. https://doi.org/10.1016/j.probengmech.2017.04.001
43. Dempster AP. Upper and lower probabilities induced by a multivalued mapping. *Ann Inst Stat Math*. 1967;38(2):325-339.
44. Shafer G. *A Mathematical Theory of Evidence*. Vol. 42. Princeton, New Jersey: Princeton University Press; 1976.
45. Klir GJ, Smith RM. On measuring uncertainty and uncertainty-based information: recent developments. *Ann Math Artif Intell*. 2001;32(1/4):5-33. https://doi.org/10.1023/A:1016784627561
46. Li D, Tang H, Xue S, Su Y. Adaptive sub-interval perturbation-based computational strategy for epistemic uncertainty in structural dynamics with evidence theory. *Prob Eng Mech*. 2018;53:75-86. https://doi.org/10.1016/j.probengmech.2018.05.001
47. Li D, Tang H, Xue S, Guo X. Reliability analysis of nonlinear dynamic system with epistemic uncertainties using hybrid Kriging-HDMR. *Prob Eng Mech*. 2019;58:1-13, 103001. https://doi.org/10.1016/j.probengmech.2019.103001
48. Bai YC, Jiang C, Han X, Hu DA. Evidence-theory-based structural static and dynamic response analysis under epistemic uncertainties. *Finite Elem Anal Des*. 2013;68:52-62. https://doi.org/10.1016/j.finel.2013.01.007
49. Tang H, Li D, Li J, Xue S. Epistemic uncertainty quantification in metal fatigue crack growth analysis using evidence theory. *Int J Fatigue*. 2017;99:163-174. https://doi.org/10.1016/j.ijfatigue.2017.03.004

50. Yang X, Liu Y, Gao Y. Unified reliability analysis by active learning Kriging model combining with random-set based Monte Carlo simulation method. *Int J Numer Methods Eng*. 2016;108(11):1343-1361. https://doi.org/10.1002/nme.5255
51. Jones DR, Schonlau M, Williamj Welch DP. Efficient global optimization of expensive black-box functions. *J Glob Optim*. 1998;13(1): 455-492. https://doi.org/10.1023/A:1008306431147
52. Lophaven SN, Nielsen HB, Søndergaard J. *DACE—A Matlab Kriging Toolbox*. Vol. 2. Technical University of Denmark, DTU; 2002. http://www2.imm.dtu.dk/pubdb/p.php?1460
53. Shimoyama K, Kawai S, Alonso JJ. Dynamic adaptive sampling based on Kriging surrogate models for efficient uncertainty quantification. In: *54th AIAA/ASME/ASCE/AHS/ASC Structures, Structural Dynamics, and Materials Conference*. Boston, MA: American Institute of Aeronautics and Astronautics; 2013.
54. Yi P, Wei K, Kong X, Zhu Z. Cumulative PSO-Kriging model for slope reliability analysis. *Prob Eng Mech*. 2015;39:39-45. https://doi.org/10.1016/j.probengmech.2014.12.001
55. Spence SMJ. Optimization of uncertain and dynamic high-rise structures for occupant comfort: an adaptive kriging approach. *Struct Saf*. 2018;75:57-66. https://doi.org/10.1016/j.strusafe.2018.05.008
56. Clough RW, Penzien J. *Dynamics of Structures*. Berkeley, CA: Computers & Structures, Inc; 2003.
57. Tajimi H. A statistical method of determing the maximum response of a building structure during an earthquake, The 2nd World Conference on Earthquake Engineering. Tokyo and Kyoto: 1960.
58. Lutes LD, Sarkani S. *Random Vibrations: Analysis of Structural and Mechanical Systems*. Burlington, MA 01803, USA: Butterworth-Heinemann; 2004.
59. FEMA P-695. *Quantification of Building Seismic Performance Factors*. Washington, DC: Federal Emergency Management Agency; 2009.
60. Tributsch A, Adam C. Evaluation and analytical approximation of Tuned Mass Damper performance in an earthquake environment. *Smart Struct Syst*. 2012;10(2):155-179. https://doi.org/10.12989/SSS.2012.10.2.155

How to cite this article: Li D, Tang H, Xue S. Robust design of tuned mass damper with hybrid uncertainty. *Struct Control Health Monit*. 2021;28(10):e2803. https://doi.org/10.1002/stc.2803

APPENDIX A

A.1 | Kriging interpolation technique

In the kriging model, the system response $y(\boldsymbol{x})$ is represented as the combination of the global trend term and the error term:

$$y(\boldsymbol{x}) = \boldsymbol{g}^{\mathrm{T}}(\boldsymbol{x})\boldsymbol{\kappa} + z(\boldsymbol{x}), \tag{A1}$$

in which $\boldsymbol{g}^{\mathbf{T}}(\boldsymbol{x})\boldsymbol{\kappa}$ offers the trend term of the kriging model. $\boldsymbol{g}(\boldsymbol{x}) = [g_1(\boldsymbol{x}), g_2(\boldsymbol{x}), ..., g_k(\boldsymbol{x})]^{\mathrm{T}}$ is the basis function and $\boldsymbol{\kappa} = [\kappa_1, \kappa_2, ..., \kappa_k]^{\mathrm{T}}$ is the coefficients vector of the regression. The residual process $z(\boldsymbol{x})$ is defined with a zero mean and the following covariance between two points $\boldsymbol{x}_1$ and $\boldsymbol{x}_2$:

$$\mathrm{Cov}(z(\boldsymbol{x}_1), z(\boldsymbol{x}_2)) = \sigma^2 R(\boldsymbol{x}_1, \boldsymbol{x}_2, \boldsymbol{\omega}), \tag{A2}$$

where $\mathrm{Cov}(\cdot)$ is the covariance operator, σ^2 is the variance of the stochastic process, and $R(\boldsymbol{x}_1, \boldsymbol{x}_2, \boldsymbol{\omega})$ is the correlation function of $\boldsymbol{x}_1$ and $\boldsymbol{x}_2$ with the parameter vector $\boldsymbol{\omega}$. Given a design of experiments of system input $\mathbf{X}_{\mathrm{D}} = \{\boldsymbol{x}_1, \boldsymbol{x}_2, ..., \boldsymbol{x}_m\}$ and a corresponding system output $\boldsymbol{y}_{\mathrm{D}} = (y_1, y_2, ..., y_m)^{\mathrm{T}}$. The fitting process of the kriging model is the estimation of the parameters vector $\boldsymbol{\varphi} = [\boldsymbol{\omega}, \boldsymbol{\kappa}, \sigma^2]^{\mathrm{T}}$. The approximation of the parameter $\boldsymbol{\omega}$ is computed by maximizing the likelihood function of the posterior distribution $y(\boldsymbol{x})$, which is converted to minimize the following equation:

$$\hat{\boldsymbol{\omega}} = \underset{\boldsymbol{\omega}}{\mathrm{argmin}} \left\{ \psi(\boldsymbol{\omega}) = |\mathbf{R}(\boldsymbol{\omega})|^{1/m} \hat{\sigma}^2 \right\}. \tag{A3}$$

With an optimal parameter $\hat{\boldsymbol{\omega}}$, the value of $R(\boldsymbol{x}_1, \boldsymbol{x}_2, \hat{\boldsymbol{\omega}})$ is determined. Then the parameter vector $\boldsymbol{\kappa}$ is given as follows:

$$\hat{\boldsymbol{\kappa}} = \left\{\mathbf{G}^{\mathrm{T}}\mathbf{R}^{-1}(\hat{\boldsymbol{\omega}})\mathbf{G}\right\}^{-1}\mathbf{G}^{\mathrm{T}}\mathbf{R}^{-1}(\hat{\boldsymbol{\omega}})\boldsymbol{y}_{\mathrm{D}}, \tag{A4}$$

in which $\mathbf{G} = \{\boldsymbol{g}(\boldsymbol{x}_1), \boldsymbol{g}(\boldsymbol{x}_2), ..., \boldsymbol{g}(\boldsymbol{x}_m)\}$. The covariance function σ^2 is approximated as follows:

$$\hat{\sigma}^2 = \frac{1}{m}(\boldsymbol{y}_{\mathrm{D}} - \mathbf{G}\hat{\boldsymbol{\kappa}})^{\mathrm{T}}\mathbf{R}^{-1}(\hat{\boldsymbol{\omega}})(\boldsymbol{y}_{\mathrm{D}} - \mathbf{G}\hat{\boldsymbol{\kappa}}). \tag{A5}$$

Then the estimation of $\boldsymbol{y}(\boldsymbol{x})$ is given by the expectation of the Gaussian process:

$$\hat{y}(\boldsymbol{x}) = \boldsymbol{g}^{\mathrm{T}}(\boldsymbol{x})\hat{\boldsymbol{\kappa}} + \boldsymbol{r}^{\mathrm{T}}(\boldsymbol{x},\hat{\boldsymbol{\omega}})\mathbf{R}^{-1}(\hat{\boldsymbol{\omega}})(\boldsymbol{y}_{\mathrm{D}} - \mathbf{G}\hat{\boldsymbol{\kappa}}). \tag{A6}$$

Additionally, the corresponding variance of $y(\boldsymbol{x})$ is obtained as follows:

$$\mathrm{var}(y(\boldsymbol{x})) = \hat{\sigma}^2\left(1 + \boldsymbol{\nu}^{\mathrm{T}}\left\{\mathbf{G}^{\mathrm{T}}\mathbf{R}^{-1}(\hat{\boldsymbol{\omega}})\mathbf{G}\right\}^{-1}\boldsymbol{\nu} - \boldsymbol{r}^{\mathrm{T}}(\boldsymbol{x},\hat{\boldsymbol{\omega}})\mathbf{R}^{-1}(\hat{\boldsymbol{\omega}})\boldsymbol{r}(\boldsymbol{x},\hat{\boldsymbol{\omega}})\right), \tag{A7}$$

where $\boldsymbol{\nu} = \mathbf{G}^{-1}\mathbf{R}\boldsymbol{r}(\boldsymbol{x},\hat{\boldsymbol{\omega}}) - \boldsymbol{g}(\boldsymbol{x})$. As shown in Equations (A6) and (A7), the predicted results of the kriging model include the expectation and variance, which can be used to define the unique Gaussian process.